1988

# A Proposed System for Determination of Percent Cloud Cover

Carol L. Emrich
*University of Central Florida*

# A PROPOSED SYSTEM FOR DETERMINATION OF PERCENT CLOUD COVER

BY

CAROL L. EMRICH
B.S., University of Maryland, 1970
M.S., University of Maryland, 1974
B.S., University of Maryland, 1985

THESIS

Submitted in partial fulfillment of the requirements
for the degree of Master of Science in Engineering
in the Graduate Studies Program
of the College of Engineering
University of Central Florida
Orlando, Florida

Spring Term
1988

ABSTRACT

A method for determining percent cloud cover by taking two consecutive images using different color contrast filters, specifically a red filter and a blue filter, is described. This method (RF/BF estimate) involves dividing the "red" image by the "blue" image, pixel by pixel, and determining the percentage of pixels in the resultant image with intensity values of one. This is the percent cloud cover. The RF/BF estimate is based on the different effects of molecule and particle scattering of electromagnetic waves in the visible portion of the spectrum. These two types of scattering, Rayleigh and Mie scattering respectively, are described as they relate to this methodology.

The RF/BF estimates are compared to visual estimates of percent cloud cover using the northern portion of 100 Central Florida skies collected during the period from January 28, 1988 to February 25, 1988. A strong correlation r=0.94 was found between the RF/BF and visual estimates. Advantages of the method are discussed along with implications and suggestions for follow-up studies.

ACKNOWLEDGEMENTS

The author wishes to thank her husband, Thomas Rozenbergs, for his continued support and encouragement throughout her seemingly never-ending education. She also wishes to thank her committee members for their guidance. Furthermore, appreciation is extended to the Florida Solar Energy Center for providing the opportunity and financial support for this study, and to Mable Flumm for contributing her word processing skills and good nature. Last but certainly not least, the author wishes to thank the Lord for providing her with the patience and perseverance to complete this project.

TABLE OF CONTENTS

LIST OF TABLES

LIST OF FIGURES

# CHAPTER I

## INTRODUCTION AND BACKGROUND

Lighting consumes more than half the total energy use of many thermally energy efficient office buildings. This is a major energy use that can be immediately replaced by solar energy as daylight, with effective savings of both energy and dollars.

Although commercial and institutional uses in Florida are the greatest consumers of electrical energy for lighting in the daytime, many Florida residences suffer from a converse problem, poorly designed fenestration systems that produce excessive solar radiant heating during some portions of the day and consequently produce substantial summer loading of air-conditioner systems.

According to a calculational procedure spelled out in the Florida model energy code, summertime solar radiant heat gain through the glazed areas of a typical Florida residence can account for 40 percent of the total annual energy consumption of the building. Proper fenestration design could greatly reduce this energy use without sacrificing good illumination performance.

Sidelighting through windows is the predominant method of daylighting the multi-story buildings which predominate

in the commercial sector in the northern states and in Europe. In the South, much commercial construction is single-story, and is therefore amenable to toplighting (skylighting), which is simpler to design, provides better illumination (when properly designed), and which can be more energy efficient due to the smaller required aperture areas.

However, because of a naturally strong human need for some visual connection with the outdoors and because of the increased worker productivity that can result, sidelighting through windows and sliding glass doors will remain an important feature of building design everywhere (McCluney 1987).

The crucial aspect is design. Ideally, the fenestration system design should be based on an optimization of energy, illumination and view. To best accomplish this, a knowledge of the angular (or directional) distribution of solar radiation incident on the building aperture is necessary. With this information, solar radiant heat gain and illumination performance of the aperture can be calculated. This distribution is directly related to the solar position and atmospheric conditions including the nature and degree of cloud cover.

Florida Solar Energy Center (FSEC) has in place a daylight availability measuring station (see Figure 1) that collects data on solar irradiances and daylight illuminance

on five orthogonal planes, from the sun only, and from the sky without the sun. Also measured is daylight illuminance inside scale models with different interiors. A special scanner or luminance mapper with nine luminance sensors at 10° altitude angle intervals has been constructed. This scanner rotates about a vertical axis under computer control and measures angular distribution of sky luminance. Sky scans are done at each 5° change in solar altitude angle and at solar noon. By rotating the luminance map of the sky to place the sun at zero azimuth angle and by analyzing only skies measured at the same solar altitude angle, the effect of the sun's movement through the sky is effectively removed from the data. The only variations remaining are due to atmospheric effects such as changing atmospheric turbidity and cloud cover. Using principal component analysis and other techniques, statistical trends in the observed variations in the sky luminance distribution can be compared with cloud cover and distribution from the sky camera or sky imager.

The present method of collecting data on cloud cover and distribution at the FSEC daylight availability measuring station includes taking pictures every hour on the half hour from 5:30 a.m. to 7:30 p.m. each day and during each sky scan. This is done with a 35 mm Nikon F3 camera with a 250 magazine back, a databack, a Fisheye lens, and a motor drive which allows a computer to control

collection times. Although data collection is automated, analysis involves manually looking at each slide to determine percent cloud cover. This method presents several problems. First, the analysis of each slide is tedious and time consuming. Secondly, this method is expensive because in addition to the cost in salary monies of the observer, there is the cost of film and processing. Thirdly, there is the problem of the lag time between the actual event (when the data were collected) and the analysis of the data, due to time required to use the entire roll of 250 exposures and the time required for the laboratory to process the film. This lag time can be as long as several weeks. A sky imaging system, shown in Figure 1 (which is still in the development phase), would alleviate these problems with the added benefit of having the data computerized, thus greatly facilitating comparison studies with other daylight availability data.

A future outcome of this project could be a variety of daylight algorithms for use in computerized simulations of the long-term energy and illumination performance of apertures in buildings. Architects, engineers and consultants could use these simulations in designing and sizing fenestrations in buildings, and designing dimming systems to compensate for naturally occurring variations in daylit spaces.

NASA has expressed an interest in methods of obtaining

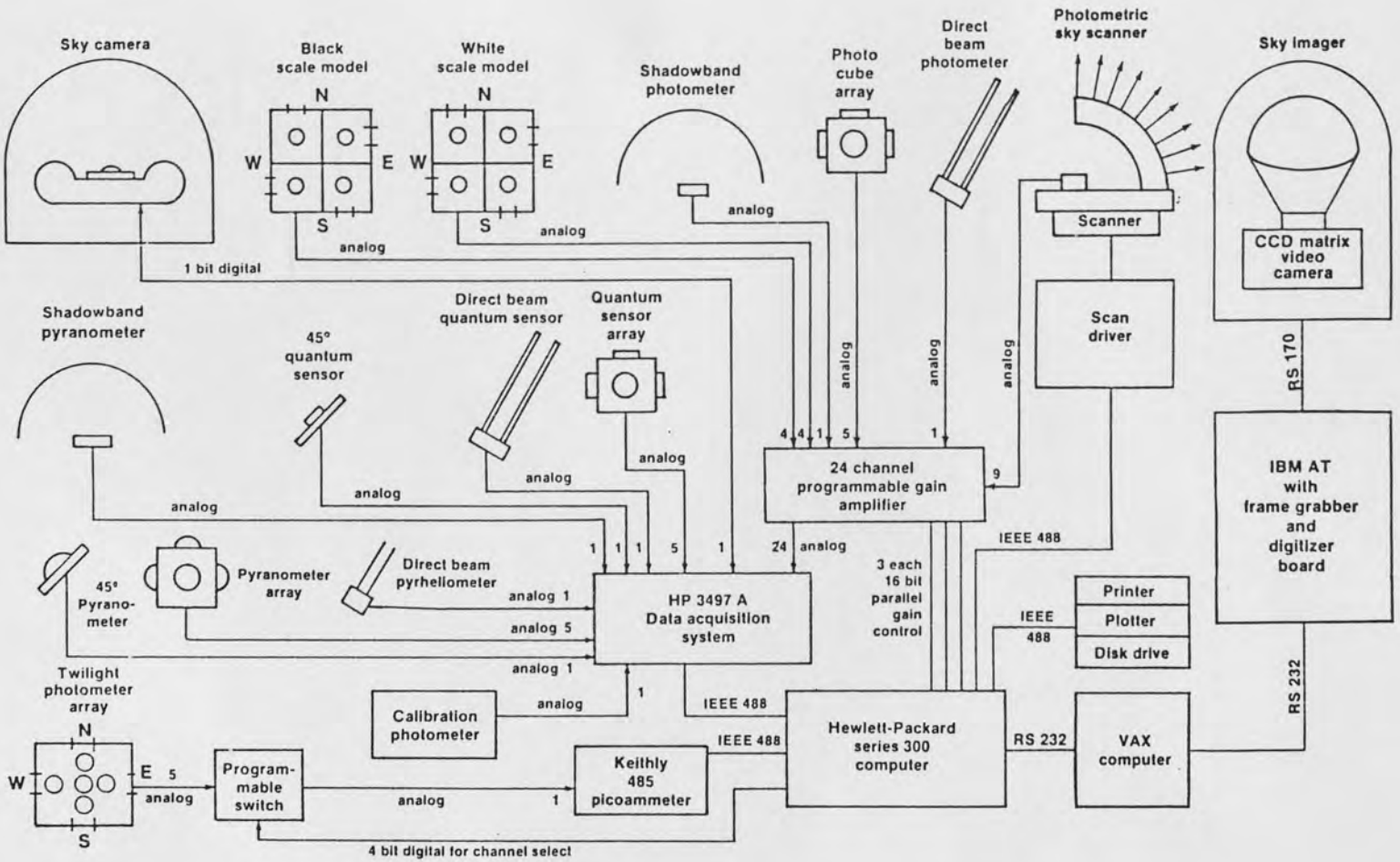


Figure 1. FSEC Daylight Availability Measuring Station.

visual cloud information in a computerized version for weather forecasting/expert systems (WFES) and other related, meteorological studies. Since our interests are closely related the possibility of a NASA/Kennedy Space Center (KSC) technology utilization (TU) project exists. Preliminary discussions with KSC personnel indicate a good potential for future funding if FSEC can demonstrate competence in this area.

Atmospheric state specifications are necessary for a number of situations including (Johnson and Hering 1987, 5):

1. Model extensions to non-uniform conditions
2. Meteorological reporting and forecasting
3. Unmanned airfield reports
4. Hostile environment monitors
5. Airborne and surface tactical planning.

Since cloud cover is a component of atmospheric state specification, an accurate automatic method for determining this variable would have numerous applications. Still to date there are relatively few ground-based systems dedicated to this purpose.

In the past records of such information have been based on eye estimates of cloud cover over the sky dome. These estimates have been and are still made at weather stations throughout the world by trained observers. In fact, eye observations remain the standard for percent

cloud cover. Absolute cloud cover can be difficult to define since clouds slant, have thickness, change shape, are at different heights, and occur at varying sun angles when seen from one point on the earth's surface. Since eye estimates are subjective and prone to human error, a more objective method using all sky photographs has been developed. Human observers tend to estimate greater than actual cloudiness by 5-10% when compared to all sky photograph interpretation. This discrepancy is due to overestimation of low clouds by the observer and omission of the outer 15% (near the horizon) of the sky in standard photograph analysis. There is also a large variation between simultaneous estimates by different observers (Holle and McKay 1975, 1441-1442). Although all-sky photograph interpretation has provided a more objective method for determining cloud cover, it is time consuming in that a observer has to interpret the photographs after the fact. Since film has to be processed before the photograph can be interpreted, the lag time between the event and the interpretation limits the applicability of this method.

Sky imaging is clearly an improvement over eye estimates and pictures. However, the best method of image processing for determining percent cloud cover has yet to be delineated. The literature on the subject consists mainly of the use of satellite-based, solid-state imaging systems.

Automatic tracking of multilayered clouds from satellite images is one of the most difficult problems in image science (Hall 1976, 118). This task requires understanding of human vision and motion perception in order to program a computer to "intelligently" process images. "Pattern recognition" is the category this type of image processing falls into. Determination of absolute cloud cover using pattern recognition from a land-based imaging system is at least equally challenging in nature. With a ground-based system the use of landmarks like lakes and coastlines to aid in cloud identification is no longer an option. The problem becomes one of differentiating between clouds and clear sky. Since clouds occur in a variety of constantly changing shapes, sizes, shades of grey, and can occur singularly, can overlap, or be multilayered, defining the patterns of clouds is a formidable task.

Edge detection is another form of image processing. An example of an edge detection procedure would be the use of a 3 x 3 convolution mask as shown below.

| | | |
|---|---|---|
| -1 | -1 | -1 |
| -1 | 9 | -1 |
| -1 | -1 | -1 |

This mask is applied to the image by multiplying each pixel grey level in a 3 x 3 pixel area of the image by the

spatially corresponding number in the mask. The grey level of the center pixel is then replaced by the sum of these nine products. If all nine pixels have the same grey level, the grey level of the center pixel will remain the same. If the surrounding grey levels of the pixels are not the same, the grey level of the center pixel will change. This procedure is continued throughout the image. The effect is that of a high-pass filter, sharpening images with high-frequency components and enhancing edges. When applied to an image of a cloudy sky, this filter not only brings out the cloud/sky borders, but the gradients within multicloud layers and within blue sky as well. Clouds frequently have very fuzzy, poorly defined edges that cannot be detected with any degree of accuracy by image processing. This type of sky with cloud imbedded in cloud background yields redundant boundaries making edge gradient techniques inaccurate and causing them to fail as the sky approaches uniform overcast.

At first glance choosing a threshold grey level and assuming that all grey levels or values of intensity higher than that would be clouds and all values lower would be blue sky seems to hold some promise. This technique could provide some degree of accuracy in a system in which an observer analyzed the image after the fact and could choose an appropriate threshold value for that particular image. However, for an automated system this poses a problem

because sky and cloud radiances vary with cloud thickness and position in relation to sun azimuth and altitude angle, necessitating continual analytical update of the threshold value based on this information. Also, dark or shadowed clouds which frequently occur on overcast and/or rainy days can mimic background sky radiances, causing this technique to be invalid in these situations (Johnson and Hering 1987, 3).

The simplest solution is based on the physical optics of light scattering in the atmosphere, specifically Rayleigh scattering and Mie scattering. Briefly stated, Rayleigh scattering involves scattering by molecules with diameters much smaller than the incident wavelength and varies with wavelength to the minus fourth power (Coulson 1975, 42). An example of this is scattering by gas molecules on a clear day giving the sky its characteristic blue color. Mie scattering involves light scattering by larger particles like water droplets which constitute a cloud or fog and has an almost constant value for visible light and droplet radii typical of clouds (Coulson 1975, 51-52). These theories are described in more detail in Chapter III. Based on these theories, clear sky and clouds could be separated using different filters. This was done at Scripps Institute of Oceanography using narrow bandpass optical filters. Specifically, a blue bandpass filter with a peak wavelength of 456 nm, and bandwidth at 0.5 peak of

56.7 nm and a red filter with a peak wavelength of 654 nm and bandwidth at 0.5 peak of 71.1 nm was used (Johnson and Hering 1987, 41). The light intensity of a clear blue sky would be greater with the blue filter than with the red filter, whereas the intensity of light from a cloud would be the same through the blue filter as it is through the red filter. Narrow bandpass optical filters can be expensive and one of the objectives is to minimize the system cost. The system should work with inexpensive color separation photographic filters as long as the cutoff for the blue filter is at a shorter wavelength than the cut-in for red filter or, in other words, they must be mutually exclusive in the visible region of the spectrum. Also the percent transmission of the two filters must be similar.

This system can be easily automated. Two consecutive images, one with a blue filter and one with a red filter, would be taken and stored. The red image would then be divided by the blue image, pixel by pixel, and the quantity rounded to the nearest integer and assigned to that same pixel. The resultant image now consists of pixels with values of either zero or one. The pixels with values of zero represent clear blue sky (intensity levels of blue filter image > intensity levels of red filter image). The pixels with values of one represent clouds, haze or fog (intensity levels of blue filter images $\cong$ intensity levels of red filter image). Finding the percentage of pixels

with a value of one will give the percentage cloud cover. The instrumentation and methodology involved are described in more detail in Chapter IV.

The objective of this thesis is to evaluate the use of color separation photographic filters in determining percent cloud cover by comparing them with visual estimates of percent cloud cover of a northern portion of a sample of 100 Central Florida skies collected from January 28, 1988 to February 25, 1988. The null hypothesis is that there will be no correlation between the two groups. The last two chapters of this thesis will include the results of this evaluation, specifically, data presentation and analysis in Chapter V and conclusions and implications in Chapter VI.

# CHAPTER II

## RADIOMETRY AND PHOTOMETRY

Sunlight incident on the earth's atmosphere is scattered by molecules and particles, giving rise to blue skies, white and grey clouds, and other phenomena such as rainbows, halos and glories. Attempts to measure the rate at which solar radiation reaches the surface of the earth have been made for more than 150 years. Only during the past few decades have these efforts begun to approach the accuracy with which other important climatic variables can be determined. Today, measurements are made with reliable instruments on satellites which are orbiting the earth far beyond the edge of the atmosphere, but, even so, the value of the solar constant (the normal incidence irradiance outside the earth's atmosphere at the average earth-sun distance) is not known precisely. There is no method presently available by which solar radiation can be measured by comparing it with some absolute standard as can be done with length and mass. Instead, a sample of incoming radiation is allowed to impinge upon a surface and then the heat or electrical effect which results is measured. This method is employed by the solid-state

camera in creating images (Yellott, 1983). In order to fully appreciate further discussion of the methodology used in this thesis and the theory it is based on, a knowledge of some basic concepts and terminology in the fields of radiometry and photometry is necessary.

Two different systems of quantification are used in describing the propagation of radiant energy and light. Radiometry deals with electromagnetic radiant energy at all wavelengths while photometry deals only with that portion of the spectrum to which the human eye is sensitive (380 to 760 nm).

The standard nomenclature has evolved over a period of half a century and has undergone numerous revisions. It incorporates the firm recommendations of the Nomenclature Committee of the Optical Society of America, as summarized by MacAdams (1967). Furthermore, it reflects general agreement with the nomenclature proposals of the International Commission on Illumination (CIE), the International Electrotechnical Commission (IEC), the International Organization for Standardization (ISO), and the SUN Commission of the International Union for Pure and Applied Physics (McCartney 1976).

## Radiometric Quantities

The radiometric quantities are listed in Table 1 along with their symbols and units. The basic symbols are the

same as those for the corresponding photometric quantities. When it is necessary to distinguish between the two, the subscript e or v is added. The first quantity in Table 1 is radiant energy Q and it depends strongly on wavelength and the spectral integral considered. This is defined by

$$Q_\lambda = \frac{dQ}{d\lambda} \qquad (2\text{-}1)$$

which means that, as the spectral interval is made indefinitely smaller, the amount of radiant energy becomes even smaller until the ratio takes on the limiting value $Q_\lambda$. Thus, $Q_\lambda$, strictly speaking, means the radiant energy per unit wavelength interval at the wavelength $\lambda$.

TABLE 1

STANDARD SYMBOLS AND UNITS OF THE RADIOMETRIC QUANTITIES (ANSI 1976)

| SYMBOL | QUANTITY | COMMON UNIT |
|---|---|---|
| Q | Radiant energy | Joule (J) |
| W | Radiant density | Joule per cubic meter ($J\ m^{-3}$) |
| $\Phi$ | Radiant flux | Watt (W) or joule per second ($J\ sec^{-1}$) |
| | Radiant flux density at a surface | |
| M | Radiant exitance (radiant emittance) | Watt per square centimeter ($W\ cm^{-2}$) |
| E | Irradiance | Watt per square meter ($Wm^{-2}$) |
| L | Radiance | Watt per square centimeter per steradian ($W\ cm^{-2}\ sr^{-1}$) Watt per square meter per steradian ($W^{-2}\ sr^{-1}$) |

Radiant density W is the electromagnetic energy content of a unit volume of space at an instant (the velocity of light) and is defined

$$W = \frac{dQ}{dV} \tag{2-2}$$

The product of energy density and velocity is the radiant power or radiant flux per unit area. Radiant flux $\Phi$ is commonly referred to as radiation, the process of initiating or sending forth electromagnetic energy by means of either waves or photons. Radiant flux is defined by

$$\Phi = \frac{dQ}{dt} \tag{2-3}$$

which expresses the time rate of energy flow past a given point. Radiant power is a synonym for radiant flux and is the quantity detected and measured by many types of sensors, including the eye. Integrating types of sensors such as photographic film, however, respond to energy, which is the product of exposure time and power.

Radiant exitance M, radiant emittance, and irradiance E describe radiant flux at a surface. The quantities are defined by

$$M \text{ or } E = \frac{d\Phi}{dA} \tag{2-4}$$

which means that, as the area is made indefinitely smaller, the amount of radiant flux also becomes smaller until the ratio takes on a limiting value. The solid angle through

which the flux leaves or reaches the surface is not specified for either quantity. In the case of emission or of diffuse reflection, the total solid angle is usually $2\pi$ steradians, or a hemisphere. In the case of irradiance, the solid angle may vary.

Radiance L applies to an extended surface which may be either an emitter or a reflector. The radiance of such a surface in any direction $\theta$ is defined as the ratio of the radiant flux leaving an element of the surface to the product of the projected area of the element and the solid angle as each of these quantities is made indefinitely small.

$$L_\theta = \frac{d^2 \Phi}{dA \cos\theta \, d\omega} \qquad (2\text{-}5)$$

This relationship is illustrated in Figure 2.

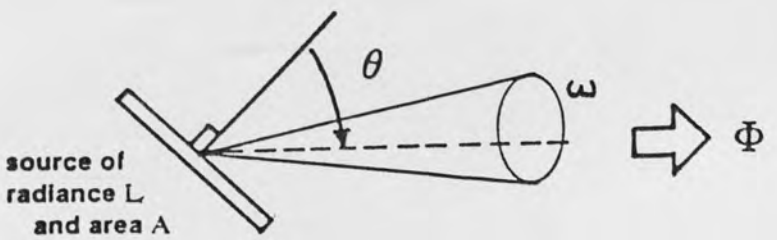


Figure 2. $L_\theta = d^2\Phi/dA\cos\theta d\omega$.

## Photometric Quantities

Photometry is the division of radiometry in which radiant flux is evaluated, not in absolute terms such as joules or watts but in terms of its ability to evoke a visual sensation. The spectral response of the human eye, according to the 1981 Reference volume of the Handbook of the Illuminating Engineering Society of North America, peaks about 555 nm and declines on either side of this peak to 50 percent at wavelengths of 510 nm and 760 nm. The bulk of the eye's sensitivity, however, lies in a more restricted portion of the spectrum from about 430 nm to 680 nm. Because the eye was the original sensor, visual considerations were paramount in the early developments of optics. Photometry preceded the larger field of radiometry. In the ultraviolet and infrared regions photoelectric and thermal sensors are essential. Instruments employing such sensors and photographic film have largely replaced the eye in photometric work, but the objective is to obtain results that agree with visual results. The eye therefore remains the ultimate judge of light in the region 380 nm to 760 nm and its response to various types and levels of stimuli are reference standards.

Table 2 lists the standard symbols and units of the photometric quantities. The symbols are the same as their corresponding quantity in the radiometric domain.

TABLE 2

STANDARD SYMBOLS AND UNITS OF THE PHOTOMETRIC QUANTITIES (ANSI 1967)

| SYMBOL | QUANTITY | COMMON UNIT |
|---|---|---|
| K | Luminous efficacy | Lumen per watt (lm $W^{-3}$) |
| V | Luminous efficiency | Numeric (0 to 1) |
| Q | Luminous energy (quantity of light) | Lumen-hour (lm-hr)<br>Lumen-second (lm-sec)<br>talbot (T) |
| W | Luminous density | Lumen-second per cubic meter (lm-sec $m^{-3}$) |
| $\Phi$ | Luminous flux<br>Luminous flux density at a surface | Lumen (lm) |
| M | Luminous exitance (luminous emittance) | Lumen per square foot (lm $ft^{-2}$) |
| E | Illuminance (illumination) | Footcandle (lm $ft^{-2}$)<br>Phot (lm/$cm^{-2}$)<br>Lux (lm $m^{-2}$) |
| L | Luminance (photometric brightness) | Candela per unit area<br>Stilb (cd $cm^{-2}$)<br>Nit (cd $m^{-2}$)<br>Lambert (cd $\pi$ $ft^{-2}$)<br>Footlambert (cd $\pi$ $cm^{-2}$)<br>Apostilb (cd $\pi$ $m^{-2}$) |

The relationship between the quantities are the same as with radiometric quantities and therefore will not be repeated in this section.

The relationship between Watts and Lumens is wavelength dependent and is called luminous efficacy K. This quantity is defined by

$$K_\lambda = \frac{d\Phi_v}{d\Phi_e} \qquad (2\text{-}6)$$

and is expressed in lumens per watt. The number of lumens

of light stimulously produced by one watt of electromagnetic radiation at the wavelength of peak visual response (555 nm) is 683. The luminous efficiency V of radiant flux is defined by

$$V_\lambda = \frac{K_\lambda}{K_{max}} \tag{2-7}$$

and has a maximum value of unity at 555 nm. $V_\lambda$ goes to zero at wavelengths of $\leq$380 nm and $\geq$760 nm.

Using the quantities of luminous efficacy and efficiency, the radiometric quantities can be related to their photometric counterpart at a specific wavelength in the following way

$$\Phi_v(\lambda) = 683 \int_{\lambda_1}^{\lambda_2} V(\lambda)\Phi_e(\lambda)d\lambda \tag{2-8}$$

$$E_v(\lambda) = 683 \int_{\lambda_1}^{\lambda_2} V(\lambda)E_e(\lambda)d\lambda \tag{2-9}$$

$$L_v(\lambda) = 683 \int_{\lambda_1}^{\lambda_2} V(\lambda)L_e(\lambda)d\lambda \tag{2-10}$$

This brief summary should assist the reader in better comprehending the remainder of this thesis.

# CHAPTER III

# LIGHT SCATTERING BY THE ATMOSPHERE

## Nature of the Scattering Process

With the radiometric terminology in mind, the basic process of scattering of a light wave incident on a particle can be considered. Scattering is the process by which a particle (any bit of matter) in the path of an electromagnetic wave continuously abstracts energy from the incident wave, and reradiates that energy into the total solid angle centered at the particle. For scattering to occur, the refractive index of the particle must be different from that of the surrounding medium. The atmospheric particles responsible for scattering range in size from gas molecules to raindrops, as listed in Table 3.

About each particle the intensity of the scattered radiant energy forms a characteristic three-dimensional pattern in space. If the scattering particle is isotropic, this pattern is symmetric about the direction of propagation of the incident beam. The shape of the pattern is dependent on the ratio of particle size to wavelength, as shown in Figure 3. The scattering is equal in the forward and backward hemispheres for particles smaller than

one tenth the wavelength of light. But, as the ratio of size to wavelength increases, the forward scattering increases with respect to the backward scattering. In all cases the form of the pattern of scattered intensity is influenced by the relative refractive index.

TABLE 3

PARTICLES RESPONSIBLE FOR ATMOSPHERIC SCATTERING
(McCartney 1976, 20)

| TYPE | RADIUS ($\mu$m) ($\mu$m) | CONCENTRATION ($cm^{-3}$) |
|---|---|---|
| Air molecule | $10^{-4}$ | $10^{-19}$ |
| Haze particle | $10^{-2}$-1 | $10^{3}$-10 |
| Fog droplet | 1-10 | 100 -10 |
| Cloud droplet | 1-10 | 300-10 |
| Raindrop | $10^{2}$-$10^{4}$ | $10^{-2}$-$10^{-5}$ |

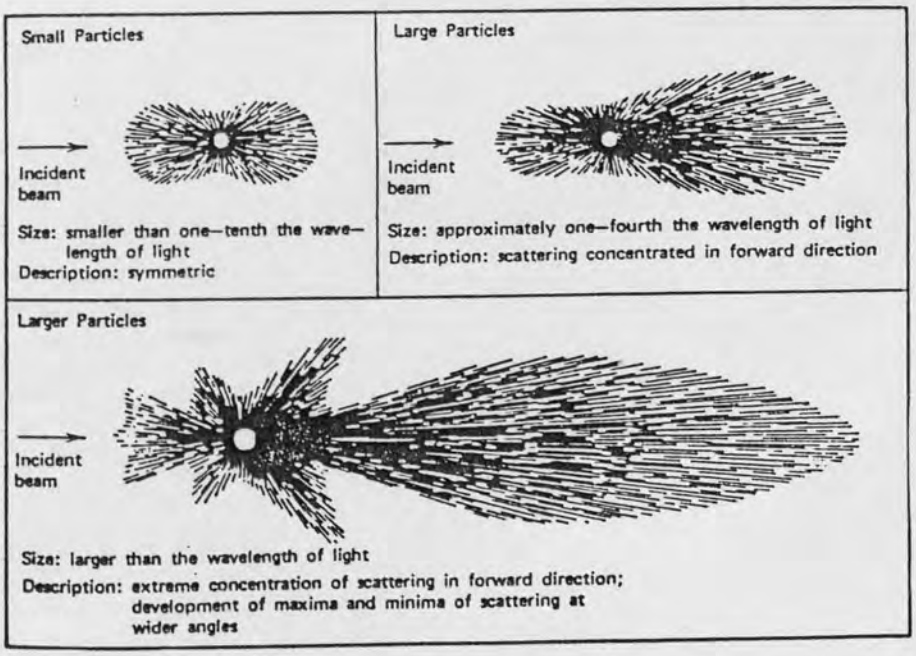


Figure 3. Angular Patterns of Scattered Intensity from Particles of Three Sizes (Brumberger et al. 1968).

The electric field of the incident or primary wave sets into oscillation the electric charges of a particle. The oscillating charges constitute one or more electric dipoles which radiate secondary, spherical waves. The secondary waves have the same frequency (and wavelength) as the primary wave, and they bear fixed phase relations to it. The scattering process is continuous.

The scattered light is polarized to some extent regardless of whether or not the incident wave is polarized. When the particle is isotropic, the polarization of the scattered intensity is a function of particle size, particle refractive index, and the wavelength of the incident light. In studies of skylight such as this thesis, angular scattering is the quantity of interest. When studying attenuation the total scattering must be considered.

The incident solar beam is transmitted directly by the atmosphere according to the Bouguer-Lambert Law (1760) which can be expressed by the following equation for a plane-parallel and horizontally homogeneous atmosphere

$$I_\lambda = I_{o\lambda} \exp(-T_\lambda \sec\theta_o)$$

where $I_{o\lambda}$ and $I_\lambda$ are the monochromatic intensities of the incident and transmitted radiations, respectively, $T_\lambda$ is the optical thickness of the atmosphere measured in the local zenith direction, and $\theta_o$ is the angle between the local zenith and the direction of the sun, and the quantity

$\sec\theta_o$ is the air mass. The optical thickness of the whole atmosphere above any arbitrary height z can be written

$$T(\lambda, z) = \int_z^\infty \beta\ (\lambda, z)dz \qquad (3\text{-}1)$$

where $\beta(\lambda,z)$ is the attenuation coefficient (Coulson 1975, 40-41).

Since attenuation is due to both scattering and absorption, subscripts are used to separate their contributions as follows:

$$\beta = \beta_{sc} + \beta_{abs} \qquad (3\text{-}2)$$

where $\beta_{abs}$ is an absorption coefficient which is analogous to the scattering coefficient $\beta_{sc}$ including the dimension length$^{-1}$. The energy associated with $\beta_{abs}$ does not in a direct sense propagate from the beam as does scattered energy. It instead raises the temperature of the medium in the first instance, with emission ultimately occurring. Since this thesis deals only with skylight (light from the sky and clouds) only $\beta_{sca}$ will be considered. Total scattering by molecules and particles are distinguished by subscripts m and p. The two effects are additive as far as attenuation is concerned (McCartney 1976, 30-31):

$$\beta_{sc} = \beta_m + \beta_p. \qquad (3\text{-}3)$$

The following sections include descriptions of molecular scattering according to Rayleigh and particle scattering according to Mie, and derivations of $\beta_m$ and $\beta_p$ as described by McCartney (1976).

## Rayleigh Scattering

Molecular scattering was described by Lord Rayleigh (J.W. Strutt, third Baron of Rayleigh) in 1871. He assumed that particles were spherical, isotropic, far smaller than the wavelength of light, and denser than the surrounding medium. Using the elastic-solid ether theory, and straight forward dimensional reasoning, he deduced that scattering varies directly as the square of the particle volume, and inversely as the fourth power of the wavelength. He showed that these atmospheric particles could not be water bubbles, but suggested they might be bits of salt.

In 1899 Rayleigh incorporated Maxwell's electromagnetic theory into his scattering theory, replacing the elastic-solid ether. He substituted refractive index for particle density. Only one emendation to his theory was necessary, and this was foreseen by Rayleigh himself and carefully investigated in the laboratory by his son, R.J. Strutt fourth Baron, and others. They found that gas molecules are not quite isotropic. Chandrasekhar (1950) extended Rayleigh's theory by developing general solutions to multiple scattering by a molecular atmosphere. Since the methodology in this thesis is based on a ratio of the effects of two types of scattering rather than an exact measure of each, it is sufficient to explain Rayleigh scattering as single scattering by an isotropic molecule.

In Rayleigh's (1899) theory, the individual molecule

is the elemental scatterer of electromagnetic waves. The molecule interacts with passing primary waves because of its electric charges or dipole nature. The primary wave is assumed to be monochromatic and linearly polarized with its electric field vector in the XY plane, as shown in Figure 4. The magnitude of the force F acting to separate nuclear and electron charges is parallel to the Y axis and is given by the product of charge e and field strength E as shown below

$$F = eE = eE_o \sin \omega t \qquad (3\text{-}4)$$

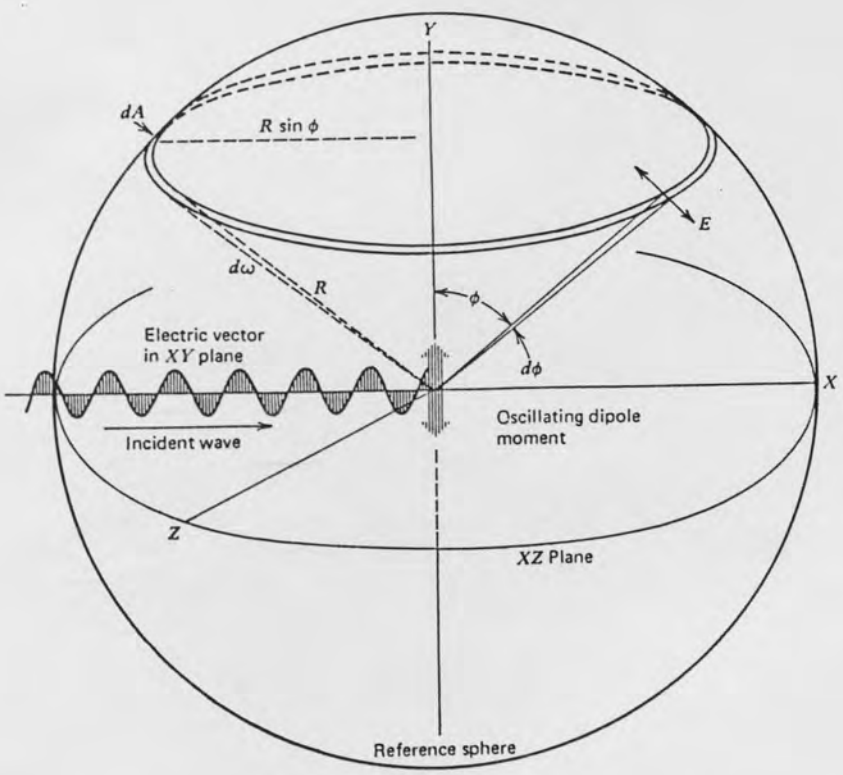


Figure 4. Geometry of Molecular Dipole Radiation (McCartney 1976, 183).

where E is the instantaneous value of the field, $E_o$ is the maximum value, t is time and $\omega$ is the electromagnetic angular frequency. The equation for motion of the electronic charge is

$$m \frac{d^2y}{dt^2} + ky = e\, E_o \sin\omega t \qquad (3\text{-}5)$$

where m is the mass of the electron, y is the displacement of the electron by the passing electromagnetic wave, and k is the restoring force per unit displacement. The steady state solution to this second order differential equation is

$$y = \frac{e}{\left[\omega_o^2 - \omega^2\right]} E_o \sin \omega t \qquad (3\text{-}6)$$

where $\omega_o$ is the vibrational (from the oscillating dipole) angular frequency. This solution is true for the displacement of charge at any given instant in time. The amplitude of the dipole formed by the oscillating negative charge and relatively stationary positive charge is equal to the product of charge and displacement

$$p = ey = \frac{e^2}{m\left[\omega_o^2 - \omega^2\right]} E_o \sin \omega t \qquad (3\text{-}7)$$

The amplitude of p follows the sinusoidal variation of the field, with a phase angle that depends on the value of $\omega$ relative to $\omega_o$. When $\omega<\omega_o$, the phase angle lies between

zero and $\pi/2$ radians, becoming equal to $\pi/2$ when $\omega=\omega_o$. The amplitude does not become infinite as the equation suggest due to the damping force which was ignored in the same equation.

The oscillating dipole moment driven by the primary wave generates a secondary wave. The radiation pattern in the immediate vicinity of the dipole is complex, but a spherical outgoing wave emerges at a distance of a few wavelengths. The electric vector of the secondary wave, according to Frank (1950), has an instantaneous amplitude of

$$E = \frac{\omega^2 \; p_o \sin\phi}{4\pi \; \epsilon_o \; c^2 \; R} \sin \omega \left[t - \frac{R}{c}\right] \qquad (3\text{-}8)$$

where $\omega$ is the electromagnetic angular frequency, t is time, $\epsilon_o$ is the permittivity of free space, $p_o$ is the maximum dipole moment, c is the speed of light, R is any distance along this direction, and $\phi$ is the angle between the dipole axis and any direction of interest.

The average power in an electromagnetic wave per unit area normal to the direction of propagation is the Poynting vector $\overline{S}$. The magnitude of this quantity is defined as

$$S = \frac{1}{2} \; c\epsilon_o E_o^2 \qquad (3\text{-}9)$$

where $E_o$ is the maximum value of the electronic field. Substituting in the value for E and assuming that the

factor $\frac{1}{2}$ takes care of the average value of the term $\sin^2\omega\left[t - \frac{R}{c}\right]$ the equation becomes

$$S = \frac{\pi^2 \, c \sin^2\phi}{2\epsilon_o \lambda^4 R^2}\left[\frac{e^2}{m\left[\omega_o^2 - \omega^2\right]}\right]^2 E_o^2 \qquad (3\text{-}10)$$

where $E_o$ is the maximum value of the electric field strength of the incident wave, $\phi$ is the scattered flux angle, m is the mass of the electron, e is the charge of the electron, and $\omega_o$ is the resonant angular frequency. Irradiance does not uniquely express the angular scattering characteristic because of the distance factor. Multiplying the previous equation by $R^2$ gives the intensity or flux per unit solid angle which is sometimes used. The intensity of the scattered flux is written

$$I(\phi) = \frac{\pi^2 \quad c \sin^2\phi}{2\epsilon_o \lambda^4}\left[\frac{e^2}{m\left[\omega_o^2 - \omega^2\right]}\right]^2 E_o^2 \qquad (3\text{-}11)$$

This is also referred to as "scattered intensity."

Relating the molecular dipole factors e, m, and $\omega$ to the refractive index of a gas in macroscopic or bulk form involves the polarizability of a gas (Chu 1967). The polarizability is related to the Lorentz-Lorentz expression and is defined

$$\frac{n^2 - 1}{n^2 + 2} \quad \frac{3\epsilon_o}{N} = \frac{e^2}{m\left[\omega_o^2 - \omega^2\right]} \qquad (3\text{-}12)$$

where n is the refractive index, and N is the number of dipole oscillators. Substituting this into equation (3-11), I ($\phi$) becomes

$$I(\phi) = \frac{9\pi^2 \epsilon_o c \sin^2\phi}{2N^2 \lambda^4} \left[ \frac{n^2 - 1}{n^2 + 2} \right]^2 E_o^2 \qquad (3\text{-}13)$$

The relationship of scattering intensity to angular scattering coefficient $\sigma_m$ is as follows

$$\sigma_m (\phi)\ S = I(\phi) \qquad (3\text{-}14)$$

Dividing $I(\phi)$ by $S = \frac{1}{2} c \epsilon_o E_o^2$ gives the angular scattering coefficient

$$\sigma_m(\phi) = \frac{9\pi^2}{N^2 \lambda^4} \left[ \frac{n^2 - 1}{n^2 + 2} \right]^2 \sin^2 \phi \qquad (3\text{-}15)$$

This equation can be simplified since the refractive index for air is only slightly greater than unity (n = 1.000293) for $\lambda$ = 0.55 and standard air, $n^2 + 2 = 3$ leaving

$$\sigma_m (\phi) = \frac{\pi^2 \left[n^2 - 1\right]^2}{N^2 \lambda^4} \sin^2 \phi \qquad (3\text{-}16)$$

The total scattering cross section $\sigma_m$ of a gas molecule is defined as that cross section of the incident wave, acted on by the molecule, having an area where power flowing across it is equal to the total power scattered in all directions or

$$\sigma_m = \int_0^{4\pi} \sigma_m(\phi)\, d\omega = \int_0^{4\pi} \frac{\pi^2 \left[n^2 - 1\right]^2}{N^2 \lambda^4} \sin^2 \phi \; d\omega \qquad (3\text{-}17)$$

where $d\omega = 2\pi \sin \phi d\phi$. When $d\omega$ is substituted into the equation and the limits of integration are changed, the equation becomes

$$\sigma_m = \frac{2\pi^3 \left[n^2 - 1\right]^2}{N^2 \lambda^4} \int_0^{\pi} \sin^3 \phi d\phi \qquad (3\text{-}18)$$

The definite integral is a standard form with a value of $-\frac{4}{3}-$. Therefore,

$$\sigma_m = \frac{8\pi^3 \left[n^2 - 1\right]^2}{3N^2 \lambda^4} \qquad (3\text{-}19)$$

is the total scattering cross section of an isotropic molecule illuminated by an incident beam of light.

The volume angular coefficient expresses angular scattering by a unit volume of gas and can be directly calculated from the angular scattering cross section. When the dipole moment at the center of the coordinates in Figure 4 is replaced with a unit volume of gas containing N isotropic molecules of the same species, the volume angular coefficient $\beta_m(\phi)$ for a linearly polarized incident beam of unit irradiance is as follows

$$\beta_m(\phi) = N\sigma_m(\phi) = \frac{\pi \left[n^2 - 1\right]^2}{N\lambda^4} \qquad (3\text{-}20)$$

The random spacings and thermal motions of the molecules are such that scattering is independent and incoherent. Since scattering is incoherent in all directions, the individual intensities are additive as indicated in equation (3-20).

For an unpolarized beam both the parallel $\parallel$ and perpendicular $\perp$ components must be considered. The relationship is

$$E = \frac{1}{2} (E_{\perp} + E_{\parallel}) \tag{3-21}$$

Let $\phi_1$ relate to $E_{\perp}$ and $\phi_2$ relate to $E_{\parallel}$ as shown in Figure 5. Incorporating this into equation (3-20) gives the following results

$$B_m [\phi_1, \phi_2] = \frac{1}{2} \frac{\pi^2 [n^2 - 1]^2}{N\lambda^4} [\sin\phi_1^2 + \sin\phi_2^2] \tag{3-22}$$

Referring to Figure 5

$$\cos^2\phi_1 + \cos^2\phi_2 = \sin^2\theta \tag{3-23}$$

or by substitution of identities

$$\sin^2\phi_1 + \sin^2\phi_2 = 1 + \cos^2\theta \tag{3-24}$$

Substituting (3-24) into (3-22) gives the following

$$\beta(\theta) = \frac{\pi^2 [n^2 - 1]^2}{2 N\lambda^4} [1 + \cos^2\theta] \tag{3-25}$$

which is the volume angular coefficient for unpolarized incident light.

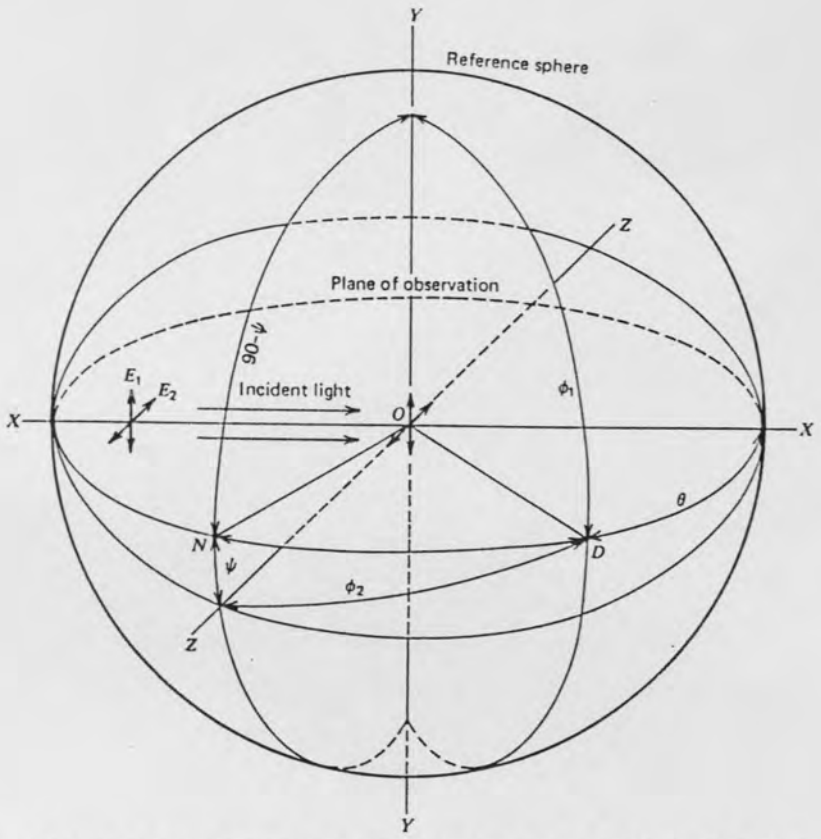


Figure 5. Geometry for the Scattering of Unpolarized Incident Light (McCartney 1967, 194).

Finally, from equations (3-20) and (3-25) total scattering coefficient $\beta_m$ can be calculated, which is the variable of interest in this thesis. In the case of polarized light, $\beta_m$ is obtained directly from equation (3-19) or by integrating (3-20) over $4\pi$ steradians yielding

$$\beta_m = \frac{8\pi^3\left[n^2 - 1\right]^2}{3N\lambda^4} \qquad (3\text{-}26)$$

For unpolarized light $\beta_m(\theta)$ (equation 3-26) is integrated over $4\pi$ steradians:

$$\beta_m = \int_o^{4\pi} \beta(\theta)\, d\omega \qquad (3\text{-}27)$$

where $d\omega = 2\pi \sin\theta d\theta$. Substituting in this quantity and equation (3-26), and changing the limits yields

$$\beta_m = \frac{\pi^3 \left[n^2 - 1\right]^2}{N \lambda^4} \int_0^{\pi} \left[1 + \cos^2\theta\right] \sin\theta d\theta \qquad (3\text{-}28)$$

The value of the definite integral is $-\frac{8}{3}$-, leaving

$$\beta_m = \frac{8\pi^3 \left[n^2 - 1\right]^2}{3N \lambda^4} \qquad (3\text{-}29)$$

which is identical to $\beta_m$ for polarized light. $\beta_m$ is defined as the ratio of the flux totally scattered in all directions, by a unit volume of gas, to the irradiance of the incident flux.

Table 4 lists some values of Rayleigh total scattering coefficients at various wavelengths for an air temperature of 288.15°K and pressure of 1013 m.b. Notice their dependence on wavelength, specifically $\lambda^{-4}$.

TABLE 4

COMPARISON OF RAYLEIGH SCATTERING COEFFICIENTS (PENNDORF 1957) AND MIE SCATTERING COEFFICIENTS (DEIRMENDJIAN 1969) AT VARIOUS WAVELENGTHS

| WAVELENGTH $\lambda$ (rm) | SCATTERING COEFFICIENT | |
|---|---|---|
| | RAYLEIGH $\beta_m$ ($m^{-1}$) | MIE $\beta_p$ ($m^{-1}$) |
| 0.45 | $2.644 \times 10^{4}$ | $1.633 \times 10^{-6}$ |
| 0.70 | $4.365 \times 10^{3}$ | $1.673 \times 10^{-6}$ |
| 1.20 | $4.976 \times 10^{3}$ | $1.729 \times 10^{-6}$ |
| 1.60 | $1.569 \times 10^{3}$ | $1.758 \times 10^{-6}$ |

## Mie Scattering

A blue sky can be explained solely on the basis of Rayleigh scattering. $\beta_m$ increases as wavelength decreases (specially as $\lambda^4$ decreases), indicating that wavelengths at the blue end of the spectrum are scattered more. This causes the sky to appear blue. Rayleigh scattering cannot however, explain effects such as haze, fog, and clouds. These optical effects are due to scattering of solar radiation by aerosol particles near the earth's surface. This type of scattering was described by Mie (1908) and includes particles whose radius is greater than 0.03 times the wavelength of light.

Scattering by a particle composed of many molecules can be treated as an extension of scattering by a single molecule. With a gas molecule only a single dipole is involved, whereas a particle consists of many closely packed complex molecules leading to an array of multipoles. Interferences among scattered waves from many closely packed molecules now can occur. The multipoles give rise to secondary electric and magnetic waves which combine in the far field to produce the scattered wave. Specifically the intensity of this scattered wave at a particular observation angle is a summation of the squares of the amplitudes of these partial waves. Since the diameter of the particle is comparable to the wavelength of the incident wave, the phase of the incident wave is not

uniform across the particle's diameter, causing interferences between the partial waves. The interferences depend on the wavelength of the incident light, the size and refractive index of the particle, and the angular location of the detector. Variations in scattered intensity between different observation angles increase as particle size increases.

For the cloud, fog, and haze aerosol, the assumption that the particle is spherical is approximately true and certainly appropriate for this thesis. The ratio of particle size to wavelength is given by

$$\alpha = \frac{2\pi r}{\lambda} \tag{3-30}$$

where $\lambda$ is the wavelength in the medium surrounding the particle and r is the radius of the particle. This dimensionless size parameter $\alpha$ is the important factor in Mie scattering rather than the absolute value of the particle size or wavelength. Also in considering refractive index, the relative value is more important than the absolute value. However, since the index of air is very close to unity (1.00029), the absolute value from 1.33 to 1.60 can be taken as the relative value.

Light scattered at the observation angle $\theta$ can be divided into perpendicularly polarized intensity $I_{\perp}$ and parallel polarized intensity $I_{\parallel}$. These components are proportional to two intensity distribution functions $i_1$

and $i_2$. These functions depend on the size parameter $\alpha$, the complex refractive index $m(\lambda) = n(\lambda) - in_i(\lambda)$, and the observation angle $\theta$. For an isotropic spherical particle these functions are written

$$i_1(\alpha,m,\theta) = \left|S_1\right|^2 = \left| \sum_{j=1}^{\infty} \frac{2j+1}{j(j+1)} \left[a_j\pi_j + b_jT_j\right] \right|^2 \qquad (3\text{-}31)$$

$$= \left|\mathrm{Re}\left[S_1\right] + \mathrm{Im}\left[S_1\right]\right|^2$$

$$i_2(\alpha,m,\theta) = \left|S_2\right|^2 = \left| \sum_{j=1}^{\infty} \frac{2j+1}{j(j+1)} \left[a_jT_j + b_j\pi_j\right] \right|^2$$

$$= \left|\mathrm{Re}\left[S_2\right] + \mathrm{Im}\left[S_2\right]\right|^2$$

where the j's are positive integers, and $S_1$ and $S_2$ are dimensionless complex amplitudes of the scattered waves observed as intensities $I_\perp(\theta)$ and $I_\parallel(\theta)$. When $\alpha \ll 1$ and $m \approx 1$, the first term in the series corresponds to Rayleigh scattering. The first partial wave (j=1) is considered to emanate from a dipole, the second partial wave from a quadrupole, and so forth. The amplitude of the jth electric partial wave is $a_j$ and the amplitude of the jth magnetic wave is $b_j$. The values of $a_j$ and $b_j$ are Ricatti-Bessel functions, whose arguments are formed from the particle characteristics $\alpha$ and m but are independent of angle $\theta$. T and $\pi$ depend only on $\theta$ and involve the first and second derivatives of Legendre polynomials having order

j and argument cosθ. Tables for the Ricatti and Bessel functions and Legendre polynomials for scattering applications have been published by Gumprecht and Sliepcevich (1951 a,b,c). The infinite series in (3-31) can be physically interpreted as a multipole expansion of scattered light. The derivation of (3-31) is beyond the scope of this thesis but can be found in several sources (Mie 1908, van de Hulst 1957, and Deirmendjian 1969).

Since irradiance E, scattering intensity I, and angular scattering coefficient $\sigma$ were thoroughly described in the section on Rayleigh scattering, specifically how the quantities are related to each other, that discussion will not be repeated in this section. Instead the derivation of the total scattering coefficient for Mie scattering, symbolized $\beta_p$, will begin with the angular cross section $\sigma_p$.

The angular cross section of a particle is analogous to that of a molecule. It is defined as the cross section of an incident wave, acted on by a particle having an area across which the power flowing is equal to the scattered power per steradian at observation angle θ. For the case where the incident beam is plane polarized with its electric vector perpendicular to the plane of observation, ($\psi$=90°) the angular cross section is written

$$\sigma_{p\perp}(\theta) = \frac{\lambda^2}{4\pi^2} i_1 \qquad (3\text{-}32)$$

Likewise for the case when $\psi=0°$

$$\sigma_{p\parallel}(\theta) = \frac{\lambda^2}{4\pi^2} i_2 \tag{3-33}$$

And finally for an incident beam of unpolarized light

$$\sigma_p(\theta) = \frac{\lambda^2}{4\pi^2} \left[ \frac{i_1 + i_2}{2} \right] \tag{3-34}$$

The volume angular coefficient $\beta_p(\theta)$ has the same form as the angular cross section $\sigma_p(\theta)$ and the two are related as follows

$$\beta_p(\theta) = N\sigma_p(\theta) \tag{3-35}$$

Thus for the three cases $\beta_p(\theta)$ is written

$$\beta_{p\perp}(\theta) = \frac{N\lambda^2}{4\pi^2} i_1 \tag{3-36}$$

$$\beta_{p\parallel}(\theta) = \frac{N\lambda^2}{4\pi^2} i_2 \tag{3-37}$$

$$\beta_p(\theta) = \frac{N\lambda^2}{4\pi^2} \left[ \frac{i_1 + i_2}{2} \right] \tag{3-38}$$

Since the dimensions of $\sigma_p(\theta)$ are $L^2$ and the dimensions of the concentration N are $L^{-3}$, the dimension of $\beta_p(\theta)$ is $L^{-1}$.

To get the total scattering coefficient $\beta_p$ equation (3-38) must be integrated with respect to $\omega$ with limits 0 to $4\pi$

$$\beta_p = \int_o^{4\pi} \beta_p(\theta)\, d\omega \qquad (3\text{-}39)$$

where $d\omega = 2\pi \sin\theta d\theta$. Making this substitution and changing the limits accordingly, the integral becomes

$$\beta_p = 2\pi \int_o^{4\pi} \beta_p(\theta) \sin\theta d\theta \qquad (3\text{-}40)$$

The integration in (3-40) is more illustrative than practical. For the purposes of computation, $\beta_p$ can be defined in terms of complex functions $a_j$ and $b_j$ (see equation 3-31) instead of $i_1$ and $i_2$ giving a total scattering coefficient of

$$\beta_p = \frac{N\lambda^2}{2\pi} \sum_{j=1}^{\infty} \left[2_j + 1\right] \left[|a_j|^2 + |b_j|^2\right] \qquad (3\text{-}41)$$

Even though it is not apparent by looking at equation (3-41), $\beta_p$ is stable over the visible portion of the spectrum. Calculated values for $\beta_p$ at the wavelengths included in Table 4 demonstrate this characteristic.

In fog, haze and cloud conditions where the particle sizes meet the criterion for Mie scattering, the intensity of the scattered wave for all wavelengths can be expected to be similar. This explains why clouds are varying shades of white to grey.

## Geometrical Optics

Light scattering by large particles can also be described using the concepts of geometric optics. The technique of ray tracing can be used in particular cases to obtain accurate numerical results for particles of size $\geq$ wavelength.

Light incident on a particle which is larger than the wavelength (size $>\lambda$) may be thought of as consisting of separate rays which pursue independent paths. If the particle size is at least several times the wavelength, it is possible to distinguish between rays striking different local regions on the particle's surface. The quantitative basis for localization of rays is contained in Huygen's concept that all points on a wavefront should be visualized as centers of secondary spherical waves. By adding to this the constraint that the secondary waves interfere according to their phase differences, Fresnel obtained a semi-quantitative description of ray localization (van de Hulst 1957, Chapter 3).

Figure 6 illustrates the terminology for the different contributions to light scattering by a large particle. In the figure $P = P_{\parallel}$ is the phase function, $\theta$ is the scattering angle, and $\gamma$ is the incident angle on the sphere for rays which strike the particle. The table on the right gives the fraction of the total scattered light contained in each value for $\ell$ for non-absorbing spheres with

refractive indices 1.33 and 2.00. Since refractive index of water is 1.33, these values would be appropriate for clouds and fog. The light rays which miss the particle ($\ell$=0) are partially diffracted into its geometric shadow.

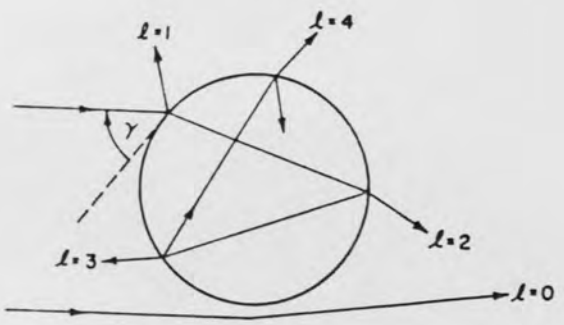


TERMINOLOGY FOR CONTRIBUTIONS TO SCATTERED LIGHT:

$\ell$

0-DIFFRACTION

1-EXTERNAL REFLECTION

2-TWICE REFRACTED RAYS

3-ONE INTERNAL REFLECTION

4-TWO INTERNAL REFLECTIONS

PHASE FUNCTION:

$$P(\theta) = \sum_{\ell=0}^{\infty} P_\ell(\theta)$$

$$\int_{4\pi} P_\ell \, d\omega/4\pi$$

| $\ell$ | $n_r$=1.33 | $n_r$=2.00 |
|---|---|---|
| 0 | .500 | .500 |
| 1 | .033 | .081 |
| 2 | .442 | .364 |
| 3 | .020 | .043 |
| 4 | .003 | .008 |
| >4 | .002 | .004 |

Figure 6. Paths of Light Rays Scattered by a Sphere According to Geometric Optics.

The intensity and polarization of the light reflected ($\ell$=1) and refracted ($\ell$>1) by the particle surface may be computed from the Fresnel reflection coefficients (Born and Wolf 1959, Sec. 13.4):

$$|R_r|^2 = \frac{(\sin\gamma - u)^2 + v^2}{(\sin\gamma + u)^2 + v^2} \tag{3-42}$$

$$|R_\ell| = \frac{\left[\left(n_r^2 - n_i^2\right)\sin\gamma - u\right]^2 + \left[2n_r n_i \sin\gamma - v\right]^2}{\left[\left(n_r^2 - n_i^2\right)\sin\gamma + u\right]^2 + \left[2n_r n_i \sin\gamma + v\right]^2} \tag{3-43}$$

where

$$u = \left[\frac{n_r^2 - n_i^2 - \cos^2\gamma + \left[\left(n_r^2 - n_i^2 - \cos^2\gamma\right)^2 + 4n_r^2 n_i^2\right]^{1/2}}{2}\right]^{1/2} \tag{3-44}$$

$$v = \left[\frac{-\left(n_r^2 - n_i^2 - \cos^2\gamma\right) + \left[\left(n_r^2 - n_i^2 - \cos^2\gamma\right)^2 + 4n_r^2 n_i^2\right]^{1/2}}{2}\right]^{1/2} \tag{3-45}$$

and $n_i$ = index of refraction of the medium of the incident ray, $n_r$ = index of refraction of the medium of the refracted ray, $|R_r|^2$ and $|R_\ell|^2$ are the reflection coefficients for the components of the intensity perpendicular and parallel, respectively, to the plane of scattering.

The rays which are refracted twice without any internal reflections ($\ell=2$) make up a large fraction of the scattered light for transparent spheres. The light which is internally reflected ($\ell\geq3$) represents no more than a few percent of the scattered light.

Light scattering calculations using geometric optics are in close agreement with calculations using Mie theory. Further comparisons of the two have been done by Hansen and Travis (1974). For this thesis Mie theory is used because

from it a scattering coefficient $\beta_p$ can be calculated and compared directly with Rayleigh scattering coefficient $\beta_m$. Therefore, any more than a brief mention of geometric optics is superfluous at this point.

## Raman Scattering

If a gas of molecules (not atoms) is irradiated by a beam of very nearly monochromatic visible or ultraviolet radiation with a mean frequency $\omega_o$ far from any resonant frequency, the weak scattered light has a spectrum consisting predominantly of a line a frequency $\omega_o$, but in addition, there are faint neighboring lines. This effect was predicted by Smekal in 1923 and experimentally demonstrated by Raman in 1928 (Stone 1963, 351). The scattered light from this effect is small enough when compared to the scattered light from Rayleigh and Mie scattering that for the purpose of this thesis it can be ignored.

## Relevance to Methodology

On a clear day the simplest atmospheric model can be used which is that of a non-absorbing medium in which all the scattering particles are much smaller in size than the wavelength of the incident beam. With this model the attenuation coefficient will consist only of $\beta_m$, so $\beta = \beta_{sc} = \beta_m$. The formula for $\beta_m$ is very wavelength

dependent ($\lambda^{-4}$), which is consistent with a clear blue sky due to increased scattering of the wavelengths at the shorter end of the visible spectrum. When an image of this clear blue sky is taken with a blue filter, the intensity levels (or grey levels) would therefore be greater than those in an image taken with a red filter.

When modeling clouds or fog as a collection of transparent spheres, all radiation which they extract from the incident beam will reappear as scattered energy. Since these water droplets which make up clouds and fog are greater in size than the wavelength of the incident beam, scattering is consistent with Mie's theory, $\beta = \beta_{sc} = \beta_p$, and has almost constant value in the visible range of wavelengths as shown in Table 4. Therefore, an image of a cloud taken with a red filter would be expected to have about the same intensity levels (or grey levels) as the same cloud imaged with a blue filter due to equal scattering at those wavelengths. As a result, when an image taken with a red filter is divided, pixel by pixel, with an image taken with a blue filter, the resultant image will consist of pixels with intensity values of either zero or one. The pixels with value of zeros represent blue sky, and those with values of one represent clouds, fog, or haze. This constitutes the theoretical basis for the method of determining percent cloud cover being evaluated in this thesis.

# CHAPTER IV

# INSTRUMENTATION AND METHODOLOGY

## Instrumentation

The imaging system for this project consists of a solid-state camera, a frame-grabbing and digitizing board installed in an IBM AT equipped with a 80287 math coprocesser, an IBM monochrome monitor, and a NEC multisync monitor for image display. Color contrast filters are used on the camera and an image processing software package facilitates image analysis. Each of these components will be described in this chapter.

### Camera

The camera is a model 5000 DATAVISION camera from Image Technology Methods Corporation, Waltham, MA. The charge-coupled device imaging matrix consists of a series of evenly spaced islands of photoconductor material deposited on a common semi-conductor surface. Shift out pixel values are continuous (at camera clock rate) and not subject to stop-start interdiction. The sensing area of the matrix is 8.8 mm x 6.6 mm and consists of a 391

(horizontal) by 491 (vertical) element array. The spectral bandwidth of the elements is from 0.4 $\mu$ to 1.2 $\mu$. The typical response curve for this type of CCD array is shown in Figure 7. Picture resolution is 280 TV lines horizontal by 350 TV lines vertical. The format of the analog output is RS 170 standard composite video with 525 lines, 60 fields/second, 30 frames/second, and 2:1 positive locked interlace scan raster. Some of the special features of this camera include: low spatial error, light bias suppression, noise rejection, dark scale reference with continually corrected scaling response, and image saturation alarm.

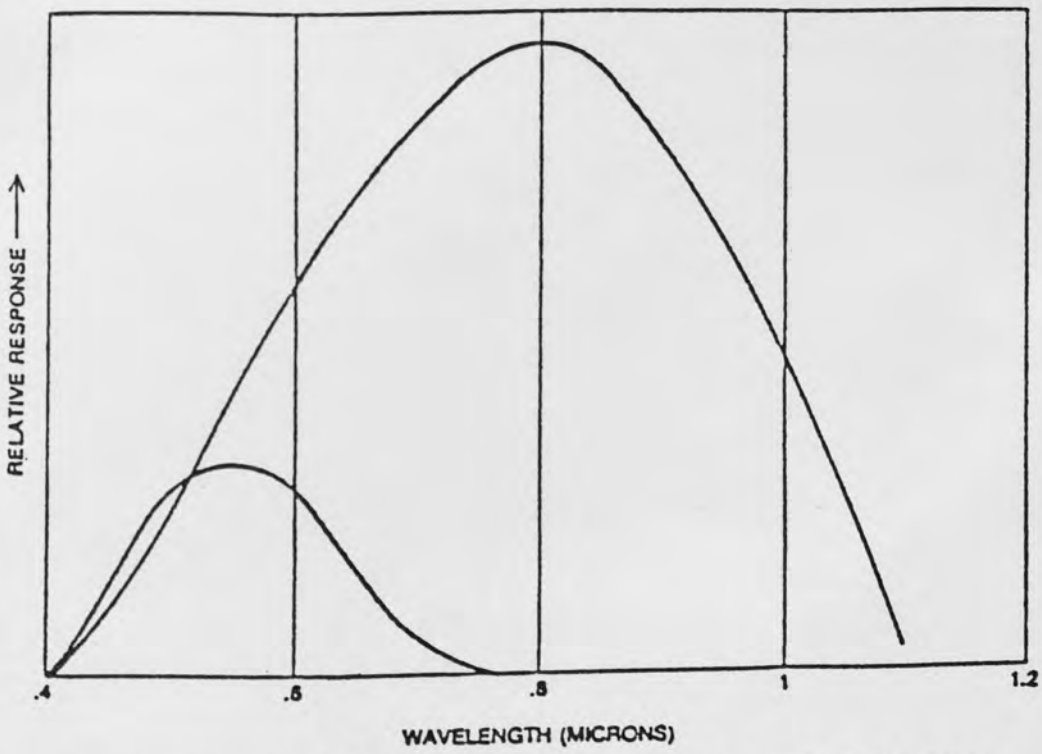


Figure 7. Relative Spectral Responses of a Charge-Coupled Silicon Photosensor Element (Large Curve) and the Human Eye (Small Curve) Are Compared.

## Lens

The lens on the camera is a SMC Pentax-A 1:1.7 50 mm lens. This lens, although standard for a 35 mm camera, is oversized for the small rectangular CCD array. The lens gives an image 24 mm x 36 mm on film; therefore, the 8.8 mm x 6.6 mm CCD array captures only a fraction of that.

## Filters

The color contrast filters are Kodak Wratten Filters. They are made by dissolving suitable organic dyes in liquid gelatin and coating the proper amount of the solution onto prepared glass. When dry, the gelatin film is stripped from the glass and coated with lacquer. These filters have a thickness of 0.1 mm plus or minus 0.01 mm. Because of their uniform thickness, gelatin filters have excellent optical quality and are well suited for precise work in which little effect on definition and no increase in optical path length can be tolerated. Each filter is standardized for spectral transmittance and total transmittance. The specific filters used were a #29 Deep Red Tricolor filter and a #47 Blue Tricolor filter. Their spectrophotometric curves are shown in Figures 8 and 9 respectively and their transmission characteristics are given in Table 2. Gelatin filters do absorb infrared radiation beginning at about 2000 nm and are fully

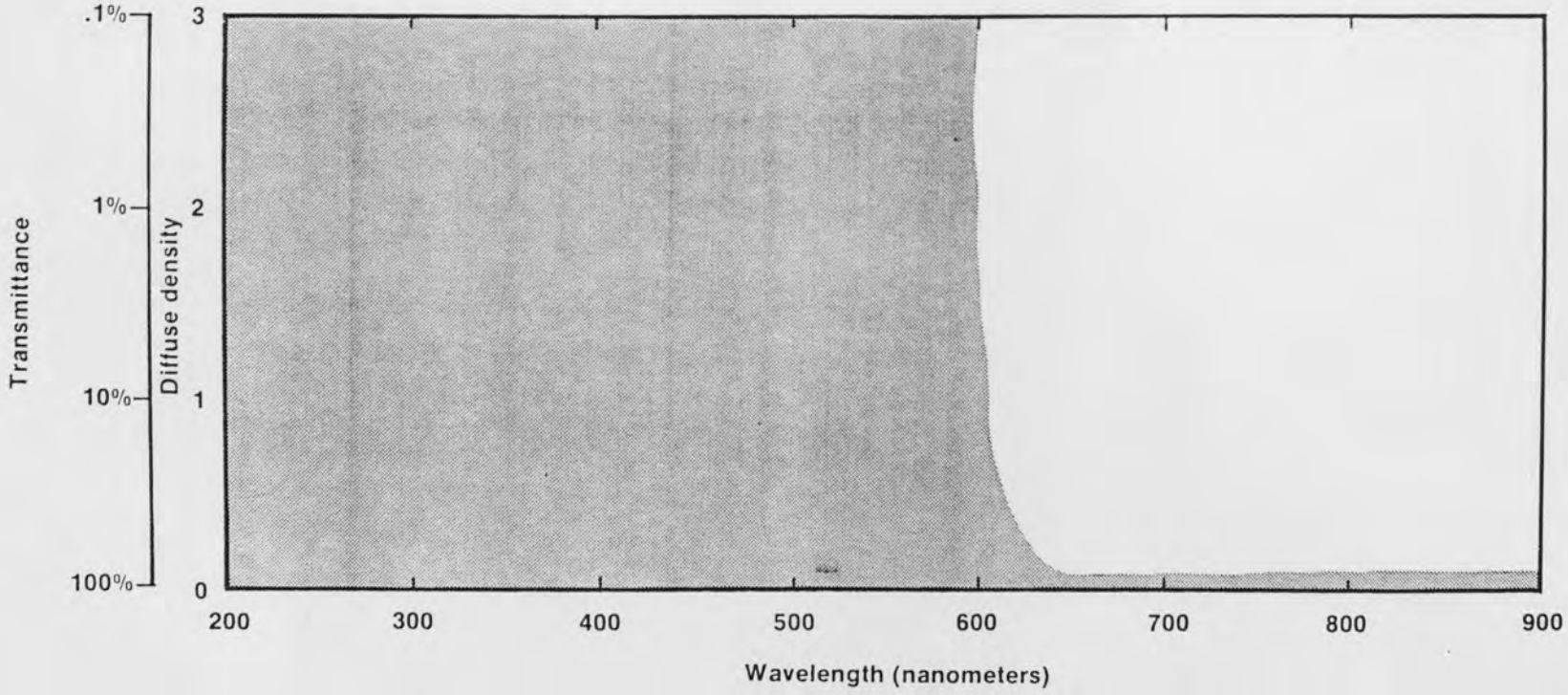


Figure 8. Kodak Wratten Gelatin Filter No. 29, deep red tricolor.
Used for color separation and tricolor printing work. Courtesy of Kodak.

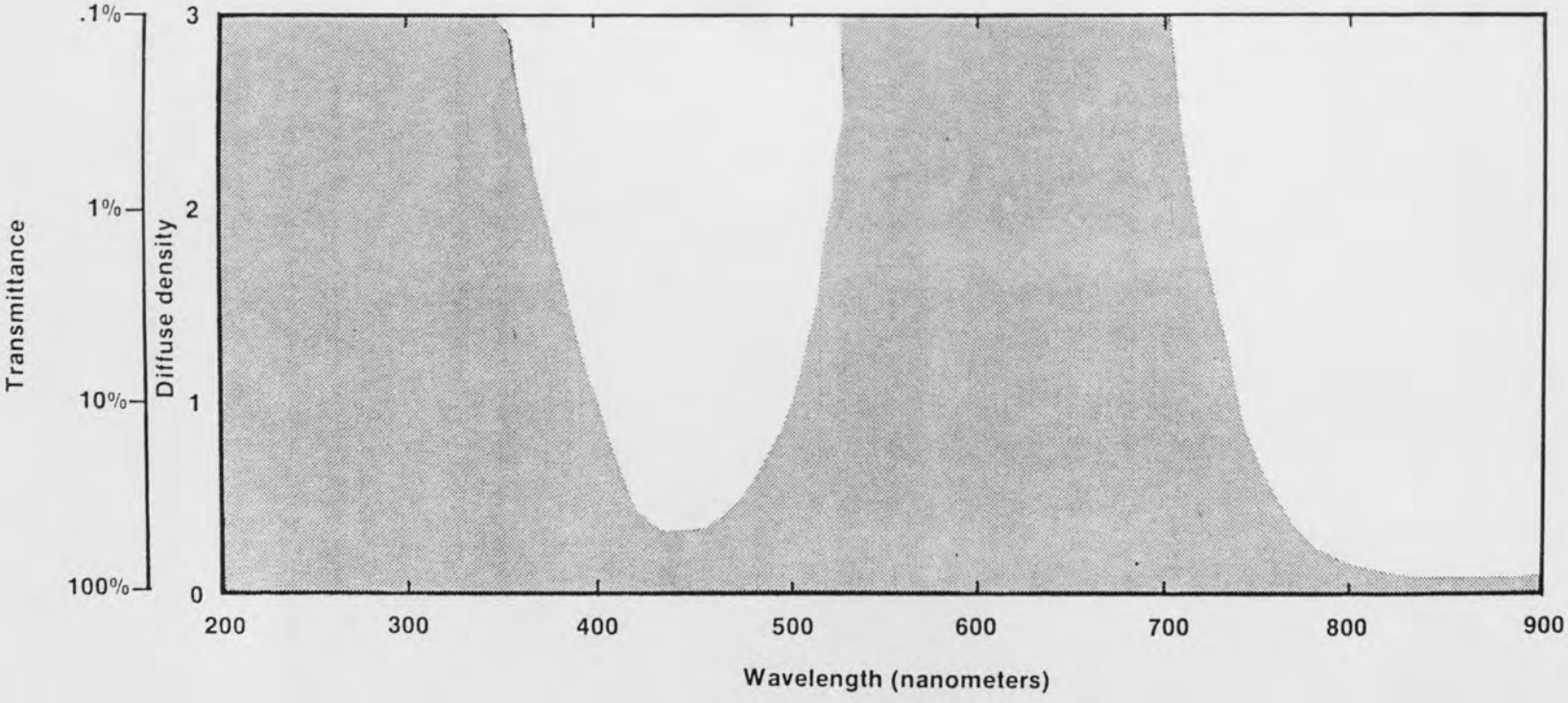


Figure 9. Kodak Wratten Gelatin Filter No. 47, blue tricolor. Used for color separation work. Courtesy of Kodak.

absorbing by about 3000 nm. These filters perform a convolution on the incoming signal from the sky.

TABLE 5

TRANSMITTANCE CHARACTERISTICS

| WAVELENGTH | PERCENT TRANSMITTANCE | |
|---|---|---|
| | NO. 29 | NO. 47 |
| 400 | -- | 9.7 |
| 410 | -- | 21.8 |
| 420 | -- | 37.8 |
| 430 | -- | 47.8 |
| 440 | -- | 50.3 |
| 450 | -- | 48.2 |
| 460 | -- | 42.8 |
| 470 | -- | 35.7 |
| 480 | -- | 27.1 |
| 490 | -- | 18.2 |
| 500 | -- | 10.2 |
| 510 | -- | 4.3 |
| 520 | -- | 1.2 |
| 530 | -- | -- |
| 540 | -- | -- |
| 550 | -- | -- |
| 560 | -- | -- |
| 570 | -- | -- |
| 580 | -- | -- |
| 590 | -- | -- |
| 600 | -- | -- |
| 610 | 10.5 | -- |
| 620 | 45.0 | -- |
| 630 | 73.5 | -- |
| 640 | 84.2 | -- |
| 650 | 87.8 | -- |
| 660 | 89.2 | -- |
| 670 | 89.8 | -- |
| 680 | 90.3 | -- |
| 690 | 90.4 | -- |
| 700 | 90.5 | -- |

## Frame Grabber

The frame grabber used in this system is a Data Translation DT2853 board for real-time digital image processing on the IBM Personal Computer AT. It is a 512 x 512 x 8-bit frame grabber that digitizes a video signal, stores an image in one of two on-board memory buffers, and displays the image in RGB false color or monochrome at a rate of 30 image frames per second. The DT2853 can also perform arithmetic and logic operations on the image in real time. The video input signal is digitized by a flash A/D converter into 8-bit pixel values for a range of 256 possible grey levels.

## Image Processing Software

The image processing software package is an interactive, mouse-driven software package for the IBM Personal Computer AT called DT/Image-Pro by Data Translation. To speed complicated image processing operations, DT/Image-Pro implements its algorithms using specialized processing hardware built into Data Translation boards. It also provides its image processing functions as FORTRAN and C-callable subroutines. These routines allow programmers to jump in and out of PC-DOS programs from the DT/Image-Pro environments.

## Methodology

The procedure involves capturing and storing two consecutive images, one with a red filter and one with a blue filter, within 25 seconds of each other. The F-stop, focus, and orientation of the camera are unchanged between the two images. The images were taken of an unobstructed portion of sky through an open, screenless, north-facing window. The portion of sky was within the 15° - 30° range above the horizon. Figure 10 shows the setup used in this procedure.

If the sky was clear or completely overcast, or the sky image was a clear or completely cloud covered portion of sky, a visual (VIS) estimate of cloud cover (0% or 100%) was recorded. Skies or portions of skies of other types were also estimated visually but with the aid of image processing techniques. The technique used depended on the type of sky. If the sky consisted only of low white clouds with distinct borders, cloud cover could be determined using the red image (RFI) and choosing a threshold grey level above which everything was clouds and below which everything was sky and then determining the percentage of pixels which were in the cloud intensity range. If the clouds were thin with unclear borders, performing either an exponential (EHE) or linear (LHE) histogram equalization on the image increased the contrast between sky and cloud on the red image.

Figure 10. Sky Imaging Setup.

An exponential histogram equalization exponentially spreads the intensity levels of the pixels over the full 256 grey levels. Compare Figures 11 and 12 to see the difference in the RFI and EHE images and their respective histograms. The actual pixel counts by grey level of the RFI and EHE are included in Appendices A and B respectively. A linear histogram equalization also spreads the intensity levels of the pixels over the full 256 grey levels, this time in a linear fashion. Compare Figures 11 and 13 to see the difference in the RFI and LHE images and their histograms. Appendix C list the pixel counts by grey level of the LHE. After using one of these methods to enhance the contrast between clouds and sky, the threshold method was employed as described previously. All of these image processing functions are part of the DT/Image-Pro software package.

After estimating percent cloud cover visually or in combination with image processing techniques, the original red image was divided by the blue image, pixel by pixel. The resultant image is composed of pixels with grey levels of either zero or one. The percentage of pixels with a value of one were calculated giving the percent cloud cover by this method.

For the clear and completely overcast sky the visual estimate was made from the actual sky and the RF/BF estimate was made from the image. The fact that the image

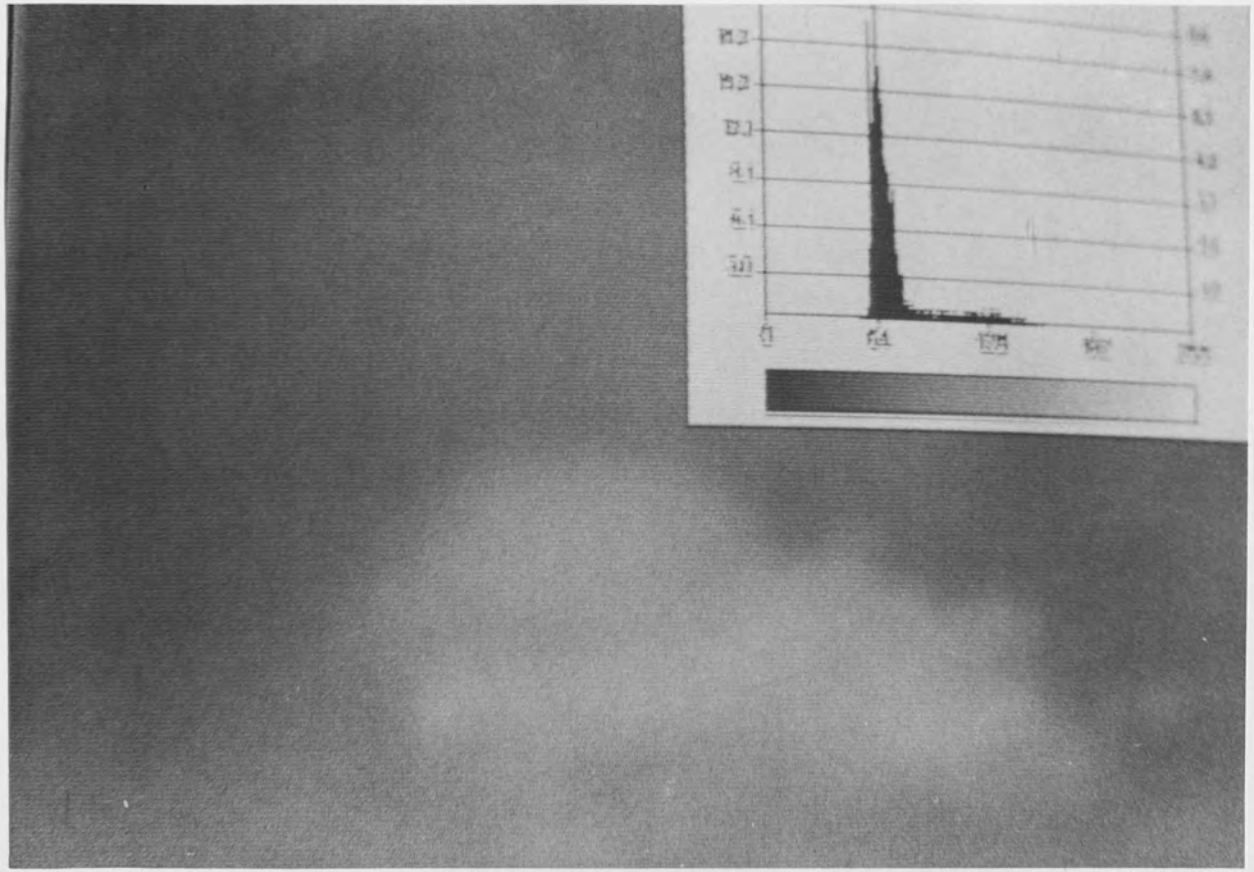

Figure 11. RFI and Histogram.

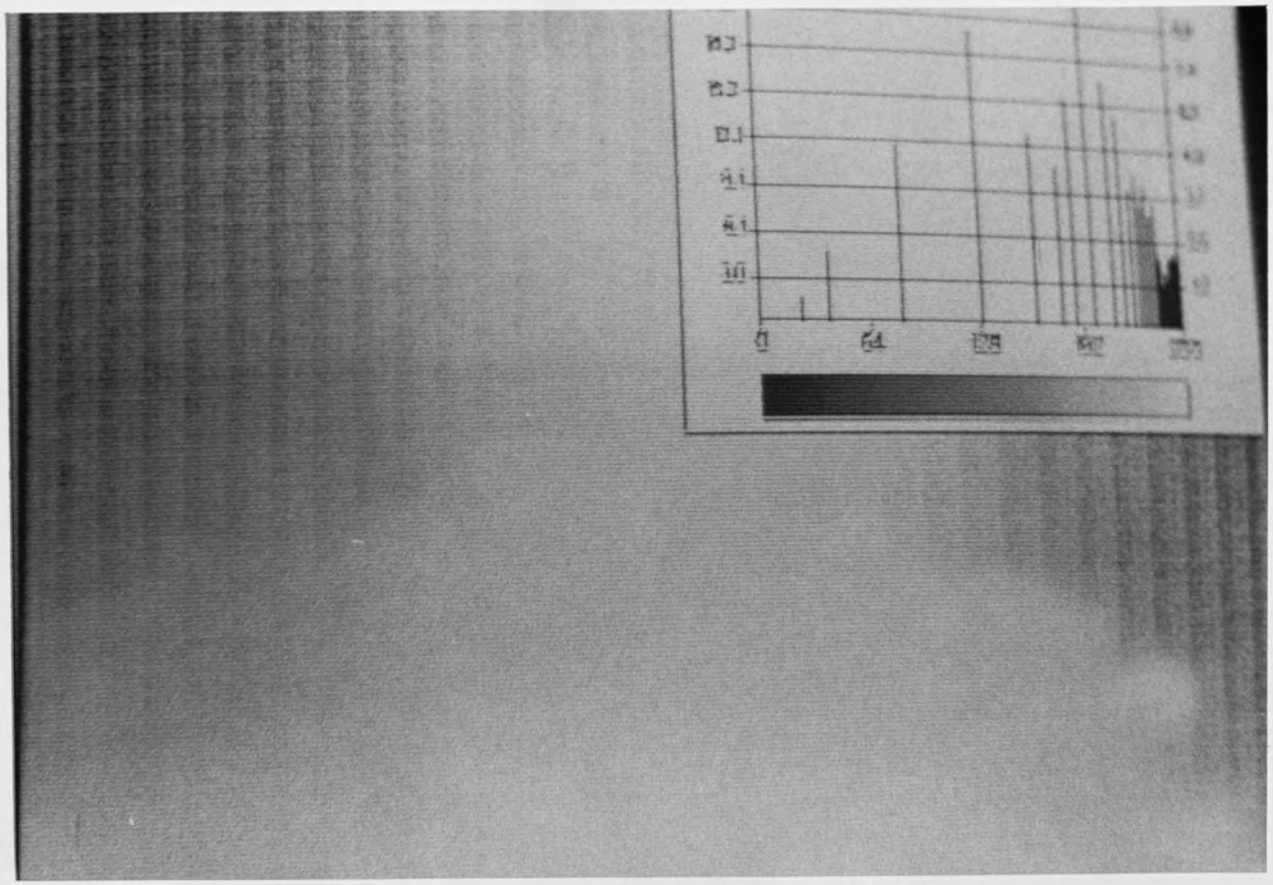

Figure 12. EHE Image and Histogram.

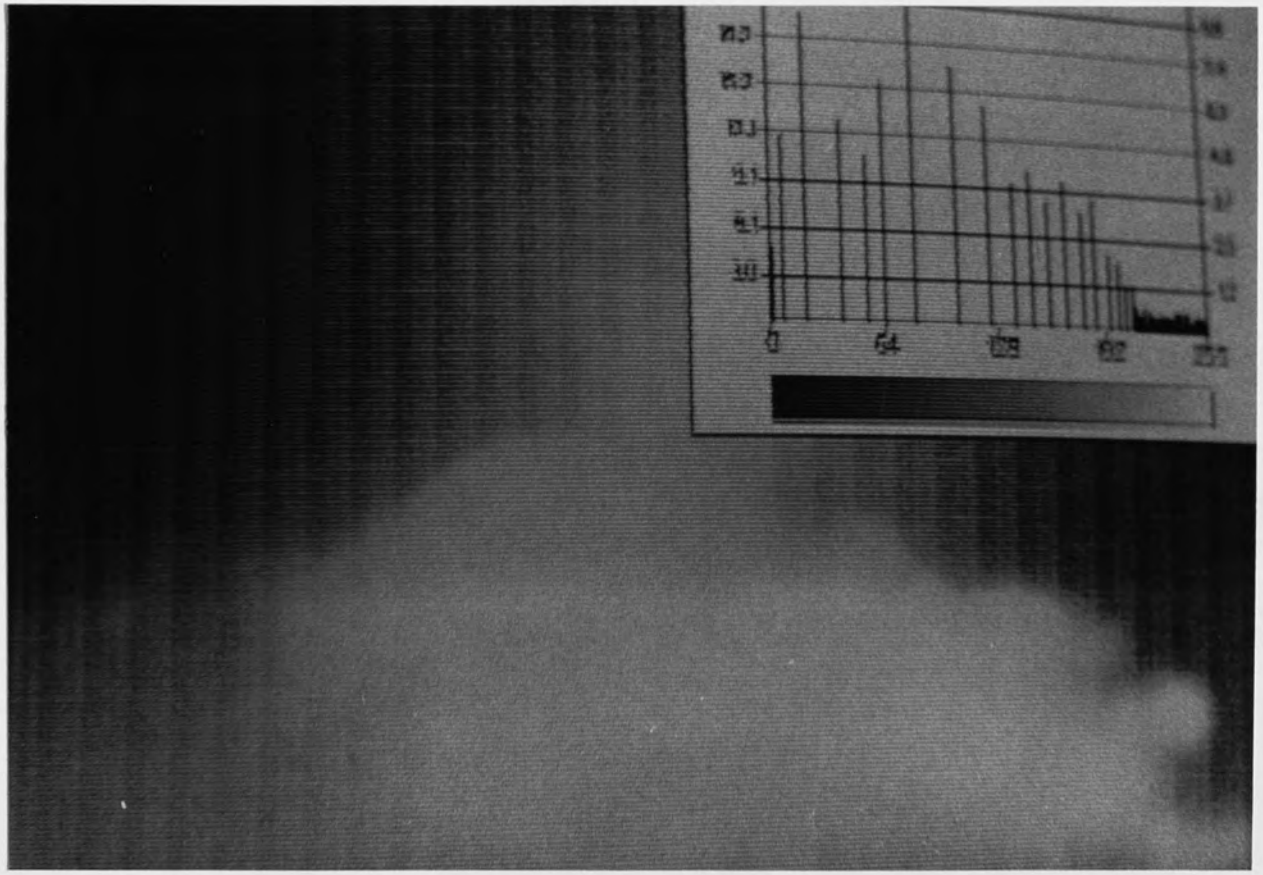

Figure 13. LHE Image and Histogram.

included only a portion of the sky was not seen as a problem in these skies because they were uniform, so cloud cover of a portion of the sky will equal that of the whole sky. For all other sky types both estimates involved a comparison of cloud cover in an image of the sky using two different methods, rather than a comparison of the actual sky and an image; therefore, calibration of the camera and correction for distortion were deemed unnecessary. A flow chart of the methodology used is included in Appendix D.

The sample of skies included any type of sky that occurred during the dates January 28, 1988 through February 25, 1988. Since real time visual estimates were necessary, sampling skies on a regularly scheduled basis would have involved dedicating a person to data collection. This was not financially feasible, so sampling was interspersed between other obligations and not done with any regularity. The maximum number of samples taken in one day was eight; the minimum was zero. Sampling was done between the hours of 7:30 a.m. and 5:30 p.m. Eastern Standard Time. The total number of skies in the population was 100.

# CHAPTER V

# DATA PRESENTATION AND ANALYSIS

## Presentation

The breakdown of the 100 skies is shown in Table 6. There were thirty-five partly cloudy (PRC), twenty-nine complete overcast (COC), twenty-five clear (CLR), six hazy (HAZ), three thin overcast (TOC), and two foggy (FOG) skies. These do not represent whole days but rather the status of the whole sky at the time the measurement was taken.

TABLE 6

BREAKDOWN OF SKY TYPES

| SKY TYPE | NO. OF SKIES |
|---|---|
| PRC | 35 |
| COC | 29 |
| CLR | 25 |
| HAZ | 6 |
| TOC | 3 |
| FOG | 2 |
| Total | 100 |

Deciding which methods to use to determine percent cloud cover for the visual estimate was a subjective decision made by the observer at the time of measurement.

Table 7 shows a breakdown of the methods used for these

TABLE 7

BREAKDOWN OF METHODS USED IN VISUAL ESTIMATES

| METHOD | NO. OF SKIES |
|---|---|
| VIS | 78 |
| RFI | 11 |
| EHE | 9 |
| LHE | 2 |
| Total | 100 |

estimates. Seventy-eight of the cases were interpreted using vision (VIS) alone; this included all of the clear, complete overcast, thin overcast, foggy, hazy, and some partly cloudy skies. The rest of the methods were used with partly cloudy skies. Eleven partly cloudy skies were interpreted by looking at the image taken with a red filter (RFI), determining the threshold grey level above which everything is clouds and below which everything is blue sky, then determining the percentage of pixels with grey levels greater than or equal to the threshold value. Nine partly cloudy skies were interpreted by enhancing the image taken with the red filter using an exponential histogram equalization (EHE) and then using the threshold method as before. The last two partly cloudy skies were interpreted using a linear histogram equalization (LHE) of the "red"

image and then using the threshold method as before. The decision whether to use RFI, EHE, or LHE was based on which method rendered an image which most resembled the actual sky. The observer's ability to discern between grey levels of similar intensity was definitely a factor in this decision. Humans can normally distinguish only ten to sixteen shades of grey. A comparison of the sensitivity of the human eye to that of the CCD array (Figure 7) displays the inequality of the two "systems."

The last table in this section of data presentation, and by far the most extensive one, is Table 8 which includes information on all 100 skies listed in chronological order. The information in the columns labeled DATE, TIME, and SKY TYPE demonstrates the changeability of Central Florida skies. Data from different days are separated by broken lines. Inspection of these columns reveals that most days include at least two different sky types, and some days include three. Even within the partly cloudy category the percent of cloud cover can vary widely as can be seen in the ESTIMATE columns. The final column labeled (RF-BF) TIME gives the time in seconds that elapsed between collection of the image with the red filter and collection of the image with the blue filter, as determined with a stop watch. Any pairs of images with separation times greater than twenty-five seconds were rejected. This was especially important

on partly cloudy days where the clouds moved quickly across the sky. Excessive picture separation times on these days could cause errors in cloud cover estimation using the

TABLE 8

SKY DATA IN CHRONOLOGICAL ORDER

| SKY # | DATE | TIME | SKY TYPE | ESTIMATE %/METHOD | RF/BF(%) | (RF-BF) TIME (SEC) |
|---|---|---|---|---|---|---|
| 1. | 1/28/88 | 12:58P | CLR | 0/VIS | 0.8 | 20.06 |
| 2. | 1/28/88 | 4:15P | HAZ | 0/VIX | 6.7 | 22.25 |
| 3. | 1/29/88 | 9:10A | COC | 100/VIS | 99.7 | 24.55 |
| 4. | 1/29/88 | 9:55A | COC | 100/VIS | 100.0 | 22.47 |
| 5. | 1/29/88 | 11:05A | COC | 100/VIS | 100.0 | 20.05 |
| 6. | 1/29/88 | 2:30P | PRC | 92.3/EHE | 97.2 | 19.60 |
| 7. | 1/29/88 | 3:05P | PRC | 93.7/EHE | 97.1 | 18.53 |
| 8. | 2/1/88 | 10:45A | HAZ | 100/VIS | 96.9 | 18.72 |
| 9. | 2/1/88 | 1:40P | TOC | 100/VIS | 99.9 | 17.52 |
| 10. | 2/1/88 | 4:45P | TOC | 100/VIS | 100.0 | 17.84 |
| 11. | 2/2/88 | 9:30A | PRC | 92/EHE | 98.2 | 23.53 |
| 12. | 2/2/88 | 9:45A | COC | 100/VIS | 100.0 | 19.78 |
| 13. | 2/2/88 | 11:00A | CLR | 0/VIS | 0.0 | 20.00 |
| 14. | 2/2/88 | 1:30P | CLR | 0/VIS | 0.0 | 20.13 |
| 15. | 2/2/88 | 3:00P | CLR | 0/VIS | 0.0 | 20.09 |
| 16. | 2/2/88 | 4:15P | CLR | 0/VIS | 0.0 | 20.97 |
| 17. | 2/2/88 | 4:45P | CLR | 0/VIS | 0.0 | 18.22 |
| 18. | 2/3/88 | 9:10A | FOG | 100/VIS | 100.0 | 18.53 |
| 19. | 2/2/88 | 10:00A | FOG | 100/VIS | 97.2 | 18.29 |
| 20. | 2/2/88 | 11:27A | PRC | 100/VIS | 97.0 | 18.06 |
| 21. | 2/2/88 | 3:30P | PRC | 53.4/LHE | 56.1 | 17.59 |
| 22. | 2/2/88 | 4:45P | PRC | 44.0/LHE | 35.9 | 16.47 |
| 23. | 2/4/88 | 8:45A | CLR | 0/VIS | 0.1 | 17.54 |
| 24. | 2/4/88 | 9:45A | CLR | 0/VIS | 2.8 | 16.38 |
| 25. | 2/4/88 | 2:20P | CLR | 0/VIS | 0.1 | 18.75 |
| 26. | 2/4/88 | 2:45P | PRC | 48.6/RFI | 44.0 | 17.50 |
| 27. | 2/4/88 | 3:15P | PRC | 84.2/RFI | 79.0 | 17.97 |
| 28. | 2/4/88 | 4:45P | PRC | 77.4/RFI | 81.9 | 17.66 |
| 29. | 2/5/88 | 8:35A | COC | 100/VIS | 100.0 | 22.22 |

TABLE 8 --CONTINUED

| SKY # | DATE | TIME | SKY TYPE | ESTIMATE %/METHOD | RF/BF(%) | (RF-BF) TIME (SEC) |
|---|---|---|---|---|---|---|
| 30. | 2/8/88 | 9:38A | COC | 100/VIS | 100.0 | 21.19 |
| 31. | 2/8/88 | 10:05A | COC | 100/VIS | 100.0 | 18.93 |
| 32. | 2/8/88 | 2:53P | COC | 100/VIS | 100.0 | 19.35 |
| 33. | 2/8/88 | 3:53P | COC | 100/VIS | 100.0 | 17.78 |
| 34. | 2/8/88 | 4:30P | COC | 100/VIS | 100.0 | 18.90 |
| 35. | 2/9/88 | 12:12P | PRC | 100/VIS | 100.0 | 20.12 |
| 36. | 2/9/88 | 4:05P | COC | 100/VIS | 100.0 | 20.72 |
| 37. | 2/9/88 | 5:05P | COC | 100/VIS | 100.0 | 19.85 |
| 38. | 2/10/88 | 7:57A | HAZ | 100/VIS | 77.0 | 18.75 |
| 39. | 2/10/88 | 2:45P | COC | 100/VIS | 100.0 | 17.13 |
| 40. | 2/10/88 | 3:24P | COC | 100/VIS | 100.0 | 16.78 |
| 41. | 2/10/88 | 4:24P | COC | 100/VIS | 100.0 | 18.62 |
| 42. | 2/10/88 | 5:05P | COC | 100/VIS | 100.0 | 18.09 |
| 43. | 2/12/88 | 11:10A | COC | 100/VIS | 100.0 | 17.87 |
| 44. | 2/12/88 | 1:10P | HAZ | 100/VIS | 89.8 | 18.09 |
| 45. | 2/12/88 | 2:08P | PRC | 93.9/RFI | 95.0 | 17.65 |
| 46. | 2/12/88 | 3:50P | CLR | 0/VIS | 0.0 | 16.97 |
| 47. | 2/12/88 | 4:35P | CLR | 0/VIS | 1.1 | 16.94 |
| 48. | 2/15/88 | 8:43A | COC | 100/VIS | 100.0 | 16.38 |
| 49. | 2/15/88 | 12:47P | PRC | 96.0/EHE | 83.2 | 17.62 |
| 50. | 2/15/88 | 2:30P | COC | 100/VIS | 100.1 | 16.74 |
| 51. | 2/15/88 | 4:05P | COC | 100/VIS | 100.0 | 16.16 |
| 52. | 2/15/88 | 5:00P | COC | 100/VIS | 100.0 | 16.94 |
| 53. | 2/16/88 | 9:30A | CLR | 0/VIS | 0.2 | 16.69 |
| 54. | 2/16/88 | 11:30A | CLR | 0/VIS | 0.0 | 15.78 |
| 55. | 2/16/88 | 1:45P | CLR | 0/VIS | 1.3 | 17.56 |
| 56. | 2/16/88 | 3:10P | CLR | 0/VIS | 0.0 | 18.36 |
| 57. | 2/16/88 | 5:10P | TOC | 100/VIS | 25.6 | 16.43 |
| 58. | 2/17/88 | 9:30A | CLR | 0/VIS | 8.0 | 18.03 |
| 59. | 2/17/88 | 10:03A | CLR | 0/VIS | 1.3 | 18.62 |
| 60. | 2/17/88 | 11:34A | PRC | 0/VIS | 14.0 | 17.87 |
| 61. | 2/17/88 | 1:30P | CLR | 0/VIS | 2.3 | 16.44 |
| 62. | 2/17/88 | 4:50P | PRC | 61.2/EHE | 58.6 | 16.44 |
| 63. | 2/18/88 | 8:45A | HAZ | 0/VIS | 69.4 | 17.69 |
| 64. | 2/18/88 | 10:00A | PRC | 84.0/EHE | 62.8 | 17.56 |
| 65. | 2/18/88 | 11:50A | PRC | 100/VIS | 97.4 | 16.19 |

TABLE 8-- CONTINUED

| SKY # | DATE | TIME | SKY TYPE | ESTIMATE %/METHOD | RF/BF(%) | (RF-BF) TIME (SEC) |
|---|---|---|---|---|---|---|
| 66. | 2/18/88 | 1:30P | PRC | 100/VIS | 99.0 | 17.88 |
| 67. | 2/18/88 | 3:15P | PRC | 21.0/RFI | 91.2 | 16.90 |
| 68. | 2/18/88 | 4:30P | PRC | 95.5/EHE | 94.5 | 18.01 |
| 69. | 2/19/88 | 9:30A | COC | 100/VIS | 100.0 | 19.16 |
| 70. | 2/19/88 | 11:09A | COC | 100/VIS | 100.0 | 16.06 |
| 71. | 2/19/88 | 2:34P | PRC | 65.8/RFI | 90.8 | 16.10 |
| 72. | 2/19/88 | 3:50P | COC | 100/VIS | 100.0 | 16.09 |
| 73. | 2/19/88 | 4:45P | PRC | 100/VIS | 100.0 | 23.03 |
| 74. | 2/22/88 | 10:30A | CLR | 0/VIS | 0.9 | 18.19 |
| 75. | 2/22/88 | 11:53A | CLR | 0/VIS | 0.8 | 16.41 |
| 76. | 2/22/88 | 1:48P | CLR | 0/VIS | 0.1 | 17.83 |
| 77. | 2/22/88 | 2:40P | PRC | 0/VIS | 0.1 | 16.63 |
| 78. | 2/22/88 | 3:30P | PRC | 17.3/RFI | 13.5 | 15.59 |
| 79. | 2/22/88 | 4:30P | PRC | 86.3/RFI | 83.0 | 16.06 |
| 80. | 2/22/88 | 4:55P | CLR | 0/VIS | 3.4 | 16.87 |
| 81. | 2/23/88 | 10:30A | PRC | 37.0/EHE | 32.2 | 16.31 |
| 82. | 2/23/88 | 11:01A | PRC | 84.8/RFI | 99.7 | 16.59 |
| 83. | 2/23/88 | 1:15P | COC | 100/VIS | 100.0 | 16.84 |
| 84. | 2/23/88 | 2:00P | COC | 100/VIS | 100.0 | 16.18 |
| 85. | 2/23/88 | 3:00P | PRC | 44.0/RFI | 98.8 | 16.69 |
| 86. | 2/23/88 | 3:37P | PRC | 100/VIS | 99.0 | 16.16 |
| 87. | 2/23/88 | 4:20P | COC | 100/VIS | 100.0 | 16.19 |
| 88. | 2/23/88 | 4:47P | COC | 100/VIS | 100.0 | 15.88 |
| 89. | 2/24/88 | 8:59A | HAZ | 100/VIS | 94.5 | 15.75 |
| 90. | 2/24/88 | 10:30A | COC | 100/VIS | 100.0 | 17.22 |
| 91. | 2/24/88 | 11:22A | PRC | 61.8/RFI | 74.6 | 15.94 |
| 92. | 2/24/88 | 12:33P | PRC | 100/VIS | 77.5 | 15.63 |
| 93. | 2/24/88 | 1:45P | PRC | 91.0/EHE | 99.8 | 17.59 |
| 94. | 2/24/88 | 3:30P | PRC | 0/VIS | 14.4 | 15.50 |
| 95. | 2/24/88 | 4:22P | PRC | 0/VIS | 22.7 | 16.28 |
| 96. | 2/25/88 | 8:50P | PRC | 0/VIS | 0.1 | 15.41 |
| 97. | 2/25/88 | 10:59A | PRC | 100/VIS | 89.8 | 16.10 |
| 98. | 2/25/88 | 1:33P | CLR | 0/VIS | 0.0 | 17.47 |
| 99. | 2/25/88 | 2:59P | CLR | 0/VIS | 0.0 | 16.51 |
| 100. | 2/25/88 | 4:22P | CLR | 0/VIS | 1.5 | 16.72 |

RF/BF method in either direction depending on the way and the speed with which the clouds were moving and/or changing shape and how quickly.

## Analysis

One method of quick comparison with this type of data is a scatterplot. Figure 14 shows the closeness of fit to the line X = Y of the RF/BF estimates to the visual estimates (includes VIS, RFI, EHE, and LHE) from Table 8. What this plot does not show is how many points an X represents. For example, the point P(X,Y) = P(0,0) represents ten estimate pairs and the point P(X,Y) = P(100,100) represents thirty-two estimate pairs. This is, however, reflected in the high correlation coefficient r = .94 (Dixon and Massey 1969, 205). Application of the student t-test to the data gives a score of t = 26.46 which indicated that the probability of the population having a correlation coefficient of zero is less than 0.1% or .001 (Dyckman, Smidt, and McAdams 1969, 495). This is the criterion for rejecting the null hypothesis and accepting the hypothesis that there is a correlation between the two methods.

The correlation between the two methods is also demonstrated by Figure 15. Using linear regression analysis, specifically the method of least squares, the

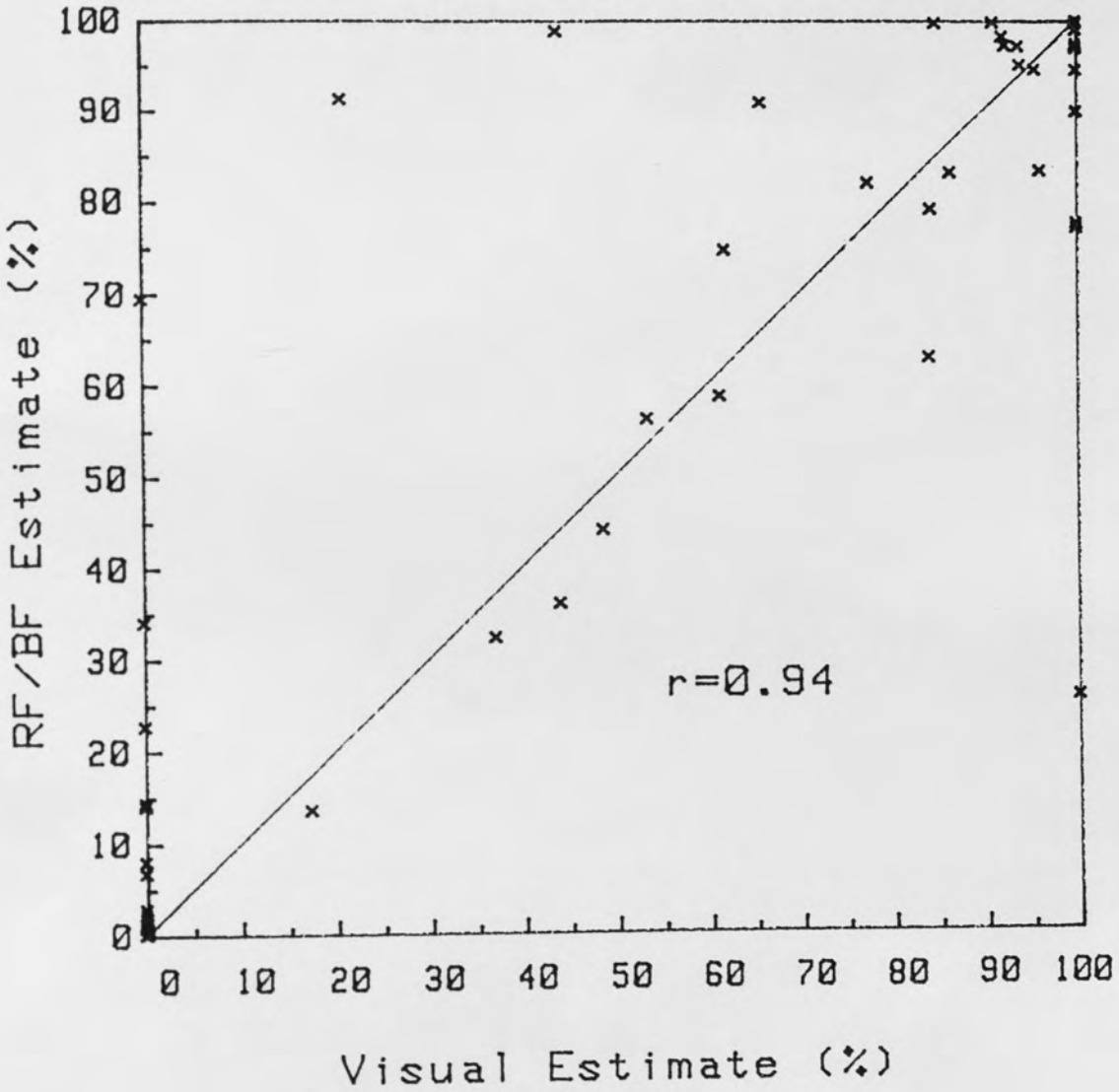


Figure 14. Scatterplot of Visual Estimate Versus RF/BF Estimate for 100 Skies Showing Closeness of Fit to Solid Line X=Y.

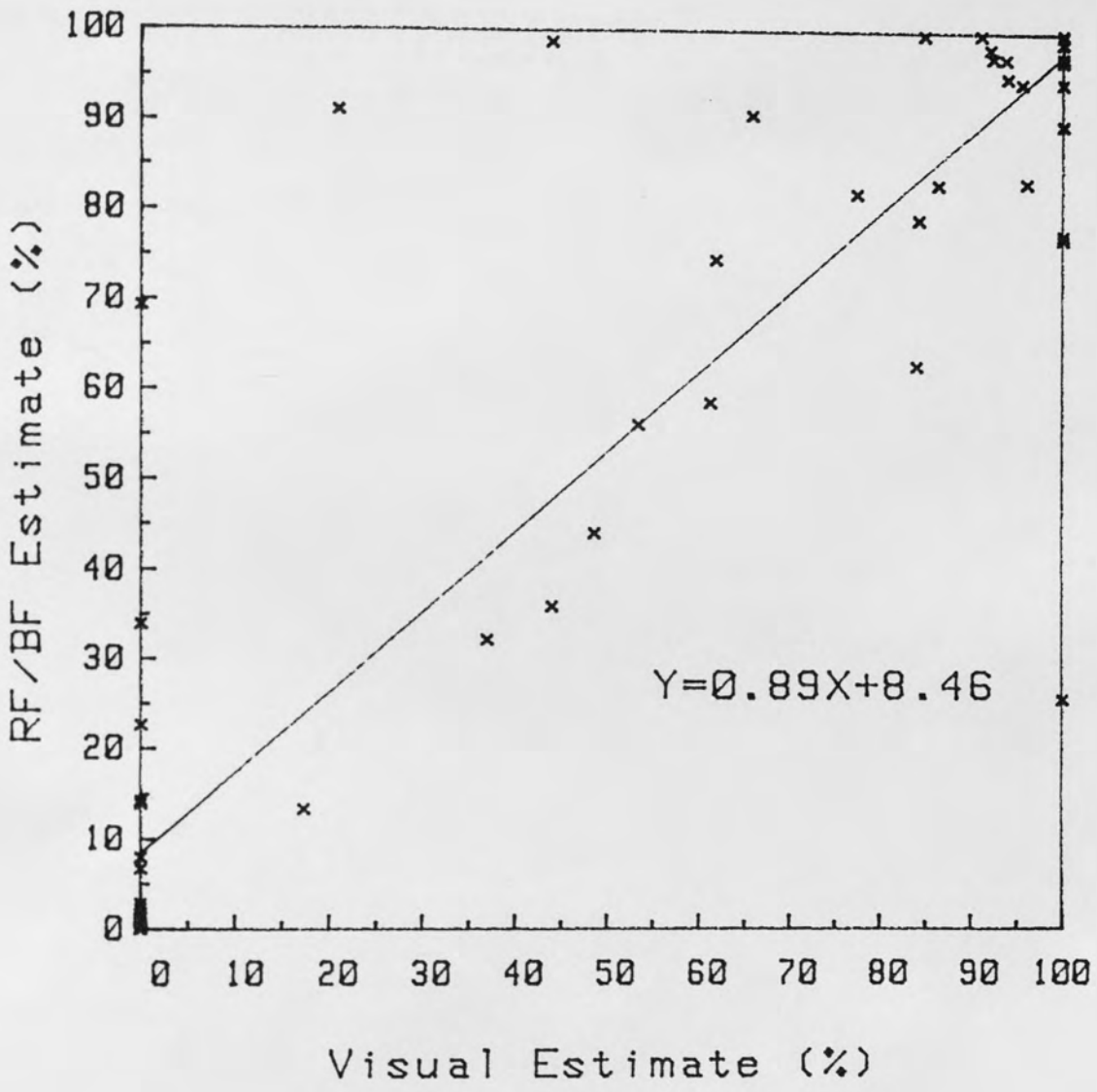


Figure 15. Scatterplot of Visual Estimate Versus RF/BF Estimate for 100 Skies with Solid Line Calculated Using Method of Least Squares.

best fitting line for the data was determined to be Y = 0.89 + 8.46 (Dixon and Massey 1969, 195).

The problem is that, since there is no standard for determining percent cloud cover other than visual observation which varies from one observer to the next, the accuracy of the visual estimates cannot be determined objectively. For that reason it is informative to divide the data into three groups: complete overcast skies, clear skies, and all other skies.

The first group includes only the complete overcast skies. In this group the visual estimates were subjectively determined to be most accurate because only skies where the observer could clearly determine that there was 100% opaque cloud cover were included in this category. Thin overcast, haze, and fog were included in the third group. Table 9 shows that for this group of twenty-nine skies, the visual estimates and the RF/BF estimates were in perfect agreement except for one sky, and that one was off by only 0.3%. The mean for the RF/BF estimates was 99.99 and the standard deviation was .005. The mean for the difference between the two estimates in each pair was .001 with a standard deviation of .006. These numbers indicate very close agreement between the two methods when the accuracy of the visual estimates was determined to be high.

TABLE 9

SKY TYPE: COMPLETE OVERCAST SKIES (N=29)
VISUAL ESTIMATE: 100% CLOUD COVER

| SKY # | NO. OF PIXELS 0 | 1 | ESTIMATE RF/BF (%) | DIFFERENCE (Y - X) |
|---|---|---|---|---|
| 3 | 773 | 244987 | 99.7 | -0.3 |
| 4 | 0 | 245760 | 100.0 | 0.0 |
| 5 | 0 | 245760 | 100.0 | 0.0 |
| 12 | 0 | 245760 | 100.0 | 0.0 |
| 29 | 0 | 245760 | 100.0 | 0.0 |
| 30 | 0 | 245760 | 100.0 | 0.0 |
| 31 | 0 | 245760 | 100.0 | 0.0 |
| 32 | 0 | 245760 | 100.0 | 0.0 |
| 33 | 0 | 245760 | 100.0 | 0.0 |
| 34 | 0 | 245760 | 100.0 | 0.0 |
| 36 | 0 | 245760 | 100.0 | 0.0 |
| 37 | 0 | 245760 | 100.0 | 0.0 |
| 39 | 0 | 245760 | 100.0 | 0.0 |
| 40 | 0 | 245760 | 100.0 | 0.0 |
| 41 | 0 | 245760 | 100.0 | 0.0 |
| 42 | 4 | 245756 | 100.0 | 0.0 |
| 43 | 0 | 245760 | 100.0 | 0.0 |
| 48 | 0 | 245760 | 100.0 | 0.0 |
| 50 | 0 | 245760 | 100.0 | 0.0 |
| 51 | 0 | 245760 | 100.0 | 0.0 |
| 52 | 9 | 245751 | 100.0 | 0.0 |
| 69 | 0 | 245760 | 100.0 | 0.0 |
| 70 | 0 | 245760 | 100.0 | 0.0 |
| 72 | 0 | 245760 | 100.0 | 0.0 |
| 83 | 0 | 245760 | 100.0 | 0.0 |
| 84 | 0 | 245760 | 100.0 | 0.0 |
| 87 | 1 | 245759 | 100.0 | 0.0 |
| 88 | 0 | 245760 | 100.0 | 0.0 |
| 90 | 0 | 245760 | 100.0 | 0.0 |
| | | | $\overline{Y}$ = 99.99<br>S.DEV.=.005 | $(\overline{Y-X})$=.001<br>S.DEV=.006 |

The second group of skies includes only the clear skies. The accuracy of visual estimates in this group was subjectively determined to be higher than the third group

but lower than the first group. This is due to the possibility of a high cloud layer too thin for the observer to see. Table 10 shows the RF/BF cloud estimates for these twenty-five skies that were visually estimated to have zero percent cloud cover. The largest difference was 8.0% in sky #58, but most of the differences were very small or zero. This is evidenced by a mean difference of 0.99 with a standard deviation of 1.75. Again, agreement in this group is very close.

The last group (Table 11) consists of all other sky types. For these forty-six skies the range of differences was from -74.4 in sky #57 to +70.2 in sky #67. Although the means of the two groups of estimates are close, $\overline{Y} = 73.50$ and $\overline{X} = 72.29$, this is mainly because the differences balance out. This is also shown by $(\overline{Y-X})=.38$. In other words, the difference is not always in the positive direction or always in the negative direction. Still, the standard deviation of this last column of numbers shows that there are substantial differences between the two estimates in this group. There are eighteen pairs with differences greater than ten, but only eight of these are greater than fifteen. The important thing to remember when considering this group of skies is that this is the group in which the visual estimates are most questionable.

TABLE 10

SKY TYPE: CLEAR SKIES (N=25)
VISUAL ESTIMATE: 0% CLOUD COVER

| SKY # | NO. OF PIXELS 0 | NO. OF PIXELS 1 | ESTIMATE RF/BF (%) | DIFFERENCE (Y - X) |
|---|---|---|---|---|
| 1 | 243901 | 1859 | 0.8 | +0.8 |
| 13 | 245760 | 0 | 0.0 | 0.0 |
| 14 | 245756 | 4 | 0.0 | 0.0 |
| 15 | 245752 | 8 | 0.0 | 0.0 |
| 16 | 245713 | 47 | 0.0 | 0.0 |
| 17 | 245659 | 101 | 0.0 | 0.0 |
| 23 | 245422 | 338 | 0.1 | +0.1 |
| 24 | 238789 | 6971 | 2.8 | +2.8 |
| 25 | 245527 | 233 | 0.1 | +0.1 |
| 46 | 245700 | 60 | 0.0 | +0.0 |
| 47 | 242951 | 2809 | 1.1 | +1.1 |
| 53 | 245357 | 403 | 0.2 | +0.2 |
| 54 | 245695 | 65 | 0.0 | 0.0 |
| 55 | 242531 | 3229 | 1.3 | +1.3 |
| 56 | 245760 | 0 | 0.0 | 0.0 |
| 58 | 226043 | 19717 | 8.0 | +8.0 |
| 59 | 242624 | 3136 | 1.3 | +1.3 |
| 61 | 240214 | 5546 | 2.3 | +2.3 |
| 74 | 243632 | 2128 | 0.9 | +0.9 |
| 75 | 243847 | 1913 | 0.8 | +0.8 |
| 76 | 245505 | 255 | 0.1 | +0.1 |
| 80 | 237465 | 8295 | 3.4 | +3.4 |
| 98 | 245751 | 9 | 0.0 | 0.0 |
| 99 | 245687 | 73 | 0.0 | 0.0 |
| 100 | 242052 | 3708 | 1.5 | +1.5 |
| | | | $\bar{Y}$ =.99 | $\overline{(Y-X)}$=0.99 |
| | | | S.DEV.=1.75 | S.DEV=1.75 |

TABLE 11

SKY TYPE: PARTLY CLOUDY (N=35), HAZY (N-6),
THIN OVERCAST (N=3), AND FOG (N=2). TOTAL N=46

| SKY #/TYPE | NO. OF PIXELS 0 | NO. OF PIXELS 1 | ESTIMATE RF/BF (%) | ESTIMATE (%)/METHOD/(Y-X) |
|---|---|---|---|---|
| 2/HAZ | 229377 | 16383 | 6.7 | 0/VIS/+ 6.7 |
| 6/PRC | 6970 | 238790 | 97.2 | 92.3/EHE/+ 4.9 |
| 7/PRC | 7228 | 238532 | 97.1 | 93.7/EHE/+ 3.4 |
| 8/HAZ | 7656 | 238104 | 96.9 | 100/VIS/- 3.1 |
| 9/TOC | 235 | 245525 | 99.9 | 100/VIS/- 0.1 |

TABLE 11 -- CONTINUED

| SKY #/TYPE | NO. OF PIXELS 0 | 1 | RF/BF (%) | ESTIMATE (%)/METHOD/(Y-X) |
|---|---|---|---|---|
| 10/TOC | 0 | 245760 | 100.0 | 100/VIS/ 0.0 |
| 11/PRC | 4412 | 241348 | 98.2 | 92.0/EHE/+ 6.2 |
| 18/FOG | 0 | 245760 | 100.0 | 100/VIS/ 0.0 |
| 19/FOG | 6943 | 238817 | 97.2 | 100/VIS/- 2.8 |
| 20/PRC | 7447 | 238313 | 97.0 | 100/VIS/- 3.0 |
| 21/PRC | 107848 | 137912 | 56.1 | 53.4/LHE/+ 2.7 |
| 22/PRC | 157580 | 88180 | 35.9 | 44.0/LHE/- 8.1 |
| 26/PRC | 137640 | 108120 | 44.0 | 48.6/RFI/- 4.6 |
| 27/PRC | 51661 | 194099 | 79.0 | 84.2/RFI/- 5.2 |
| 28/PRC | 44494 | 201266 | 81.9 | 77.4/RFI/+ 4.5 |
| 35/PRC | 0 | 245760 | 100.0 | 100/VIS/ 0.0 |
| 38/HAZ | 56480 | 189280 | 77.0 | 100/VIS/-23.0 |
| 44/HAZ | 25173 | 220587 | 89.8 | 1009VIS/-10.2 |
| 45/PRC | 12408 | 233352 | 95.0 | 93.9/RFI/+ 1.1 |
| 49/PRC | 41297 | 204463 | 83.2 | 96.0/RFI/-12.8 |
| 57/TOC | 182950 | 62810 | 25.6 | 100/VIS/-74.4 |
| 60/PRC | 211382 | 34378 | 14.0 | 0/VIS/+14.0 |
| 62/PRC | 101850 | 143910 | 58.6 | 61.2/EHE/- 1.6 |
| 63/HAZ | 75209 | 170551 | 69.4 | 100/VIS/-30.6 |
| 64/PRC | 91422 | 154338 | 62.8 | 84.0/EHE/-21.2 |
| 65/PRC | 6355 | 239405 | 97.4 | 100/VIS/- 2.6 |
| 66/PRC | 2434 | 243326 | 99.0 | 100/VIS/- 1.0 |
| 67/PRC | 21599 | 224161 | 91.2 | 21.0/RFI/+70.2 |
| 68/PRC | 13615 | 232145 | 94.5 | 95.5/EHE/- 1.0 |
| 71/PRC | 22575 | 223184 | 90.8 | 65.8/RFI/+25.0 |
| 73/PRC | 0 | 245760 | 100.0 | 100/VIS/ 0.0 |
| 77/PRC | 245576 | 184 | 0.1 | 0/VIS/+ 0.1 |
| 78/PRC | 212663 | 33097 | 13.5 | 17.3/RFI/- 3.8 |
| 79/PRC | 41890 | 203970 | 83.0 | 86.3/RFI/+ 3.3 |
| 81/PRC | 166678 | 79082 | 32.2 | 37.0/EHE/- 4.8 |
| 82/PRC | 648 | 245112 | 99.7 | 84.8/RFI/+14.9 |
| 85/PRC | 3057 | 242703 | 98.8 | 44.0/RFI/+54.8 |
| 86/PRC | 2340 | 243420 | 99.0 | 100/VIS/- 1.0 |
| 89/HAZ | 13500 | 232260 | 94.5 | 100/VIS/- 5.5 |
| 91/PRC | 62469 | 183291 | 74.6 | 61.8/RFI/+12.8 |
| 92/PRC | 55239 | 190521 | 77.5 | 100/VIS/-22.5 |
| 93/PRC | 437 | 245323 | 99.8 | 91.0/EHE/+ 8.8 |
| 94/PRC | 210473 | 35287 | 14.4 | 0/VIS/+14.4 |
| 95/PRC | 189896 | 55864 | 22.7 | 0/VIS/+22.7 |
| 96/PRC | 245435 | 325 | 0.1 | 0/VIS/+ 0.1 |
| 97/PRC | 25097 | 220663 | 89.8 | 100/VIS/-10.2 |
| | | | $\bar{Y}$=72.50 | $\bar{X}$=72.29//($\overline{Y-X}$)=.38 |
| | | | S.DEV.=32.9 | S.DEV=72.50//S.DVE=20.35 |

# CHAPTER VI

# CONCLUSIONS AND IMPLICATIONS

The purpose of this study was to investigate whether the RF/BF method of percent cloud cover determination is at least as accurate as visual estimation. The RF/BF method involves taking two consecutive images with a red color contrast filter and blue color contrast filter, respectively, dividing the "red" image by the "blue" image pixel by pixel, and determining in what percentage of pixels the intensity levels of the two images were alike (resultant pixel value equal to one). The visual estimates were done by simple visual observation in the case where the portion of the sky either had no clouds or all clouds, or visual observation of the RF image before or after image enhancement depending on the degree of contrast in intensity levels in the original image.

A comparison of these two methods on a northern portion of 100 Central Florida skies from January 28, 1988 to February 25, 1988, revealed that the two methods gave comparable results on this population of skies. The correlation coefficient between these two methods was r =

0.94. Application of the student's t-test showed that the chance of obtaining the calculated value of r for a true value of $r = 0$ is $< 0.1\%$, indicating a strong correlation between each pair of cloud cover estimates.

The agreement was greatest for complete overcast skies where the two estimates were exactly the same in twenty-eight of the twenty-nine skies. Only skies in which there was no blue sky visible, only opaque clouds, were included in this group. Thin translucent clouds were included in another group of skies. Therefore, the visual cloud cover in this group of skies was deemed very reliable. Thus the greatest agreement between the two methods was in the group of skies where the visual estimate was determined to be most accurate. One possible interpretation of this finding would be that the RF/BF method may be more accurate than the visual method. This would be a logical assumption given that the CCD array in the camera is much more sensitive than the eye (Figure 7). This interpretation would also be supported by the finding that the second highest agreement was in the clear group of skies which is the next most reliable group as far as visual estimates go.

The only skies included in the clear sky group were skies in which there was no haze, fog, or cloud cover discernible by visual observation. The uncertainty comes with the high, thin translucent cloud layer that may be missed by the eye. Still, agreement in this group of

twenty-five skies was very close with the largest difference being eight percent.

The last group of skies included all other types of skies. This group includes the most difficult skies to analyze by visual observation -- those with a high, thin, translucent cloud layer, those with haze, and/or indistinct cloud/sky borders. Problems of perspective and projection, as well as the subjective nature of eye estimates of cloud cover, all come into play here. The latter weakness of the human observer was demonstrated in the study made by Galligan (1953) in which several trained observers independently estimated cloud cover. The variability in estimating total cloud amount was greatest for values around 50%. Galligan concluded that for a true cloud cover of 0.5, ninety-five percent of the observer reports can be expected to lie between 0.25 and 0.75. This could explain some of the large differences in this last group of skies. The other problem is the inability to quantify haze in terms of cloud cover. The visual estimate would be either zero or one hundred percent whereas the RF/BF estimate will quantify the haze based on electromagnetic scattering by the particles.

The standard to date for percent cloud cover determination is still eye observations. For this reason this study compared the RF/BF method to visual observations. The obvious question is how accurate are

visual observations? This is an issue which needs to be addressed further. A comprehensive study, comparing all existing methods, radar, radiometric, RF/BF, threshold method, infrared, along with independent estimates of several trained observers would be interesting but unfortunately too expensive to undertake at this laboratory setting. Even if this study were undertaken and a new objective method of determining percent cloud cover were adopted, what about cloud classification, and interpretation with the intent of forecasting weather conditions? It is doubtful that any one objective method of cloud cover determination could replace the human weather observer.

For the purposes of this laboratory, which is concerned mainly with daylight availability and its correlation with percent cloud cover, the RF/BF method shows promise. It needs to be tested with a fisheye lens assembly to focus the image of the entire sky onto the small CCD array. Implementation of an automatically tracking disk to block the CCD array from the sun and circumsolar element at all times plus an automatic filter changer would also be necessary. The last two items would be computer controlled, as would sky image collection times. For accurate percent cloud cover estimates, correction for distortion from the lens assembly and digitization would be necessary.

Once this system was fully automated and protected in a weather-proof housing, the entire sky could be evaluated on a regular basis for percent cloud cover. Simultaneous, side-by-side pictures with a 35 mm camera could be used for comparison. With this setup a sampling of Central Florida skies at regular intervals throughout all four seasons could be achieved. This would be the next logical step in evaluation of this RF/BF method.

If the same high correlation coefficients were obtained from all-sky testing of the RF/BF method versus visual estimation (this time using 35 mm photographs), then the method could be accepted as an automated method for determination of percent cloud cover. The advantages are the availability of real-time results and the obvious savings in time and money compared to the other visual methods, which require either an observer dedicated to making scheduled real-time observations of the sky, or after-the-fact analysis of all-sky photographs or slides.

Another variation on this theme would be to use a color camera with photoconducting elements with different spectral sensitivities. Pixels with like intensity levels in the red and blue portion of the spectrum would represent cloud, whereas high blue, low red would be sky. This would eliminate the need for two consecutive images and an automatic filter wheel.

Analysis of different cloud types using fast fourier transforms would make another interesting study. The assumption is that this analysis may lead to an automatic method for cloud typing.

Implications for an automated system to determine percent cloud cover extend beyond this laboratory for possible use in meteorological reporting and forecasting, and unmanned surface and/or airborne reports and tactile planning. Other uses include correlation studies comparing percent cloud cover to daylight availability. A future outcome could be a variety of daylight algorithms for use in computerized simulations of long-term energy and illumination performance of apertures in buildings.

# APPENDIX A

# PIXEL COUNTS BY GREY LEVEL

# OF RFI

| Mean | Mode | Median | Std Dev |
|---|---|---|---|
| 75 | 66 | 68 | 19.928 |

| Index | 0 | 10 | 20 | 30 | 40 |
|---|---|---|---|---|---|
| 0 | 0 | 0 | 0 | 0 | 0 |
| 1 | 0 | 0 | 0 | 0 | 0 |
| 2 | 0 | 0 | 0 | 0 | 0 |
| 3 | 0 | 0 | 0 | 0 | 0 |
| 4 | 0 | 0 | 0 | 0 | 0 |
| 5 | 0 | 0 | 0 | 0 | 0 |
| 6 | 0 | 0 | 0 | 0 | 0 |
| 7 | 0 | 0 | 0 | 0 | 0 |
| 8 | 0 | 0 | 0 | 0 | 0 |
| 9 | 0 | 0 | 0 | 0 | 0 |

| Index | 50 | 60 | 70 | 80 | 90 |
|---|---|---|---|---|---|
| 0 | 0 | 4781 | 10356 | 1176 | 706 |
| 1 | 2 | 11961 | 8405 | 942 | 538 |
| 2 | 5 | 19996 | 9582 | 1110 | 614 |
| 3 | 25 | 12979 | 7758 | 806 | 580 |
| 4 | 181 | 10799 | 8469 | 864 | 723 |
| 5 | 177 | 15633 | 5033 | 640 | 486 |
| 6 | 143 | 24277 | 4474 | 771 | 559 |
| 7 | 182 | 16817 | 2917 | 566 | 375 |
| 8 | 222 | 14465 | 2779 | 680 | 518 |
| 9 | 664 | 9301 | 1628 | 461 | 491 |

| Index | 100 | 110 | 120 | 130 | 140 |
|---|---|---|---|---|---|
| 0 | 604 | 611 | 752 | 850 | 394 |
| 1 | 487 | 395 | 552 | 691 | 291 |
| 2 | 672 | 423 | 765 | 919 | 473 |
| 3 | 551 | 409 | 455 | 626 | 307 |
| 4 | 597 | 648 | 650 | 852 | 333 |
| 5 | 412 | 444 | 556 | 488 | 279 |
| 6 | 543 | 696 | 825 | 586 | 431 |
| 7 | 409 | 521 | 456 | 389 | 334 |
| 8 | 547 | 705 | 438 | 470 | 395 |
| 9 | 434 | 488 | 463 | 336 | 258 |

| Index | 150 | 160 | 170 | 180 | 190 |
|---|---|---|---|---|---|
| 0 | 296 | 93 | 0 | 0 | 0 |
| 1 | 155 | 63 | 0 | 0 | 0 |
| 2 | 204 | 105 | 0 | 0 | 0 |
| 3 | 137 | 43 | 0 | 0 | 0 |
| 4 | 176 | 33 | 0 | 0 | 0 |
| 5 | 122 | 5 | 0 | 0 | 0 |
| 6 | 202 | 1 | 0 | 0 | 0 |
| 7 | 107 | 0 | 0 | 0 | 0 |
| 8 | 123 | 0 | 0 | 0 | 0 |
| 9 | 68 | 0 | 0 | 0 | 0 |

| Index | 200 | 210 | 220 | 230 | 240 |
|---|---|---|---|---|---|
| 0 | 0 | 0 | 0 | 0 | 0 |
| 1 | 0 | 0 | 0 | 0 | 0 |
| 2 | 0 | 0 | 0 | 0 | 0 |
| 3 | 0 | 0 | 0 | 0 | 0 |
| 4 | 0 | 0 | 0 | 0 | 0 |
| 5 | 0 | 0 | 0 | 0 | 0 |
| 6 | 0 | 0 | 0 | 0 | 0 |
| 7 | 0 | 0 | 0 | 0 | 0 |
| 8 | 0 | 0 | 0 | 0 | 0 |
| 9 | 0 | 0 | 0 | 0 | 0 |

| Index | 250 | 260 | 270 | 280 | 290 |
|---|---|---|---|---|---|
| 0 | 0 | | | | |
| 1 | 0 | | | | |
| 2 | 0 | | | | |
| 3 | 0 | | | | |
| 4 | 0 | | | | |
| 5 | 0 | | | | |
| 6 | | | | | |
| 7 | | | | | |
| 8 | | | | | |
| 9 | | | | | |

# APPENDIX B

# PIXEL COUNTS BY GREY LEVEL

# OF EHE

| Mean | Mode | Median | Std Dev |
|---|---|---|---|
| 200 | 198 | 219 | 52.014 |

| Index | 0 | 10 | 20 | 30 | 40 |
|---|---|---|---|---|---|
| 0 | 0 | 0 | 0 | 0 | 4781 |
| 1 | 0 | 0 | 0 | 0 | 0 |
| 2 | 0 | 0 | 0 | 0 | 0 |
| 3 | 0 | 0 | 0 | 0 | 0 |
| 4 | 0 | 0 | 1601 | 0 | 0 |
| 5 | 0 | 0 | 0 | 0 | 0 |
| 6 | 0 | 0 | 0 | 0 | 0 |
| 7 | 0 | 0 | 0 | 0 | 0 |
| 8 | 0 | 0 | 0 | 0 | 0 |
| 9 | 0 | 0 | 0 | 0 | 0 |

| Index | 50 | 60 | 70 | 80 | 90 |
|---|---|---|---|---|---|
| 0 | 0 | 0 | 0 | 0 | 0 |
| 1 | 0 | 0 | 0 | 0 | 0 |
| 2 | 0 | 0 | 0 | 0 | 0 |
| 3 | 0 | 0 | 0 | 11961 | 0 |
| 4 | 0 | 0 | 0 | 0 | 0 |
| 5 | 0 | 0 | 0 | 0 | 0 |
| 6 | 0 | 0 | 0 | 0 | 0 |
| 7 | 0 | 0 | 0 | 0 | 0 |
| 8 | 0 | 0 | 0 | 0 | 0 |
| 9 | 0 | 0 | 0 | 0 | 0 |

| Index | 100 | 110 | 120 | 130 | 140 |
|---|---|---|---|---|---|
| 0 | 0 | 0 | 0 | 19996 | 0 |
| 1 | 0 | 0 | 0 | 0 | 0 |
| 2 | 0 | 0 | 0 | 0 | 0 |
| 3 | 0 | 0 | 0 | 0 | 0 |
| 4 | 0 | 0 | 0 | 0 | 0 |
| 5 | 0 | 0 | 0 | 0 | 0 |
| 6 | 0 | 0 | 0 | 0 | 0 |
| 7 | 0 | 0 | 0 | 0 | 0 |
| 8 | 0 | 0 | 0 | 0 | 0 |
| 9 | 0 | 0 | 0 | 0 | 0 |

| Index | 150 | 160 | 170 | 180 | 190 |
|---|---|---|---|---|---|
| 0 | 0 | 0 | 0 | 0 | 0 |
| 1 | 0 | 0 | 0 | 0 | 0 |
| 2 | 0 | 0 | 0 | 0 | 0 |
| 3 | 0 | 12979 | 0 | 0 | 0 |
| 4 | 0 | 0 | 0 | 0 | 0 |
| 5 | 0 | 0 | 0 | 0 | 0 |
| 6 | 0 | 0 | 0 | 0 | 0 |
| 7 | 0 | 0 | 0 | 15633 | 0 |
| 8 | 0 | 0 | 10799 | 0 | 24277 |
| 9 | 0 | 0 | 0 | 0 | 0 |

| Index | 200 | 210 | 220 | 230 | 240 |
|---|---|---|---|---|---|
| 0 | 0 | 0 | 0 | 0 | 8469 |
| 1 | 0 | 16817 | 0 | 0 | 0 |
| 2 | 0 | 0 | 0 | 8405 | 5033 |
| 3 | 0 | 0 | 0 | 0 | 4474 |
| 4 | 0 | 0 | 0 | 9582 | 2917 |
| 5 | 0 | 0 | 9301 | 0 | 2779 |
| 6 | 0 | 0 | 0 | 0 | 3746 |
| 7 | 0 | 0 | 0 | 7758 | 3420 |
| 8 | 0 | 0 | 10356 | 0 | 4916 |
| 9 | 0 | 14465 | 0 | 0 | 3756 |

| Index | 250 | 260 | 270 | 280 | 290 |
|---|---|---|---|---|---|
| 0 | 4652 | | | | |
| 1 | 3626 | | | | |
| 2 | 4888 | | | | |
| 3 | 5198 | | | | |
| 4 | 4432 | | | | |
| 5 | 4743 | | | | |
| 6 | | | | | |
| 7 | | | | | |
| 8 | | | | | |
| 9 | | | | | |

# APPENDIX C

# PIXEL COUNTS BY GREY LEVEL

# FOR LHE

| Mean | Mode | Median | Std Dev |
|---|---|---|---|
| 122 | 81 | 124 | 76.145 |

| Index | 0 | 10 | 20 | 30 | 40 |
|---|---|---|---|---|---|
| 0 | 0 | 0 | 19996 | 0 | 12979 |
| 1 | 1601 | 0 | 0 | 0 | 0 |
| 2 | 4781 | 0 | 0 | 0 | 0 |
| 3 | 0 | 0 | 0 | 0 | 0 |
| 4 | 0 | 0 | 0 | 0 | 0 |
| 5 | 0 | 0 | 0 | 0 | 0 |
| 6 | 0 | 0 | 0 | 0 | 0 |
| 7 | 11961 | 0 | 0 | 0 | 0 |
| 8 | 0 | 0 | 0 | 0 | 0 |
| 9 | 0 | 0 | 0 | 0 | 0 |

| Index | 50 | 60 | 70 | 80 | 90 |
|---|---|---|---|---|---|
| 0 | 0 | 0 | 0 | 0 | 0 |
| 1 | 0 | 0 | 0 | 24277 | 0 |
| 2 | 0 | 0 | 0 | 0 | 0 |
| 3 | 0 | 0 | 0 | 0 | 0 |
| 4 | 10799 | 0 | 0 | 0 | 0 |
| 5 | 0 | 15633 | 0 | 0 | 0 |
| 6 | 0 | 0 | 0 | 0 | 0 |
| 7 | 0 | 0 | 0 | 0 | 0 |
| 8 | 0 | 0 | 0 | 0 | 0 |
| 9 | 0 | 0 | 0 | 0 | 0 |

| Index | 100 | 110 | 120 | 130 | 140 |
|---|---|---|---|---|---|
| 0 | 0 | 0 | 0 | 0 | 0 |
| 1 | 0 | 0 | 0 | 0 | 0 |
| 2 | 0 | 0 | 0 | 0 | 0 |
| 3 | 0 | 0 | 0 | 0 | 0 |
| 4 | 0 | 0 | 14465 | 0 | 0 |
| 5 | 0 | 0 | 0 | 0 | 0 |
| 6 | 16817 | 0 | 0 | 0 | 0 |
| 7 | 0 | 0 | 0 | 0 | 0 |
| 8 | 0 | 0 | 0 | 0 | 10356 |
| 9 | 0 | 0 | 0 | 9301 | 0 |

| Index | 150 | 160 | 170 | 180 | 190 |
|---|---|---|---|---|---|
| 0 | 0 | 0 | 0 | 0 | 0 |
| 1 | 0 | 0 | 0 | 0 | 0 |
| 2 | 0 | 0 | 0 | 0 | 0 |
| 3 | 0 | 0 | 0 | 0 | 0 |
| 4 | 0 | 0 | 0 | 0 | 0 |
| 5 | 0 | 0 | 0 | 0 | 5033 |
| 6 | 0 | 0 | 0 | 8469 | 0 |
| 7 | 0 | 0 | 0 | 0 | 0 |
| 8 | 0 | 9582 | 7758 | 0 | 0 |
| 9 | 8405 | 0 | 0 | 0 | 0 |

| Index | 200 | 210 | 220 | 230 | 240 |
|---|---|---|---|---|---|
| 0 | 4474 | 1628 | 1167 | 952 | 650 |
| 1 | 0 | 0 | 538 | 981 | 1381 |
| 2 | 0 | 1176 | 1194 | 1006 | 894 |
| 3 | 0 | 942 | 723 | 832 | 1313 |
| 4 | 0 | 1110 | 1045 | 1092 | 691 |
| 5 | 2917 | 0 | 893 | 696 | 919 |
| 6 | 0 | 1670 | 1095 | 1226 | 626 |
| 7 | 0 | 640 | 1159 | 1240 | 852 |
| 8 | 2779 | 771 | 551 | 552 | 1074 |
| 9 | 0 | 1246 | 1009 | 1220 | 859 |

| Index | 250 | 260 | 270 | 280 | 290 |
|---|---|---|---|---|---|
| 0 | 1021 | | | | |
| 1 | 1113 | | | | |
| 2 | 1044 | | | | |
| 3 | 949 | | | | |
| 4 | 794 | | | | |
| 5 | 843 | | | | |
| 6 | | | | | |
| 7 | | | | | |
| 8 | | | | | |
| 9 | | | | | |

# APPENDIX D

# FLOW CHART OF METHODOLOGY

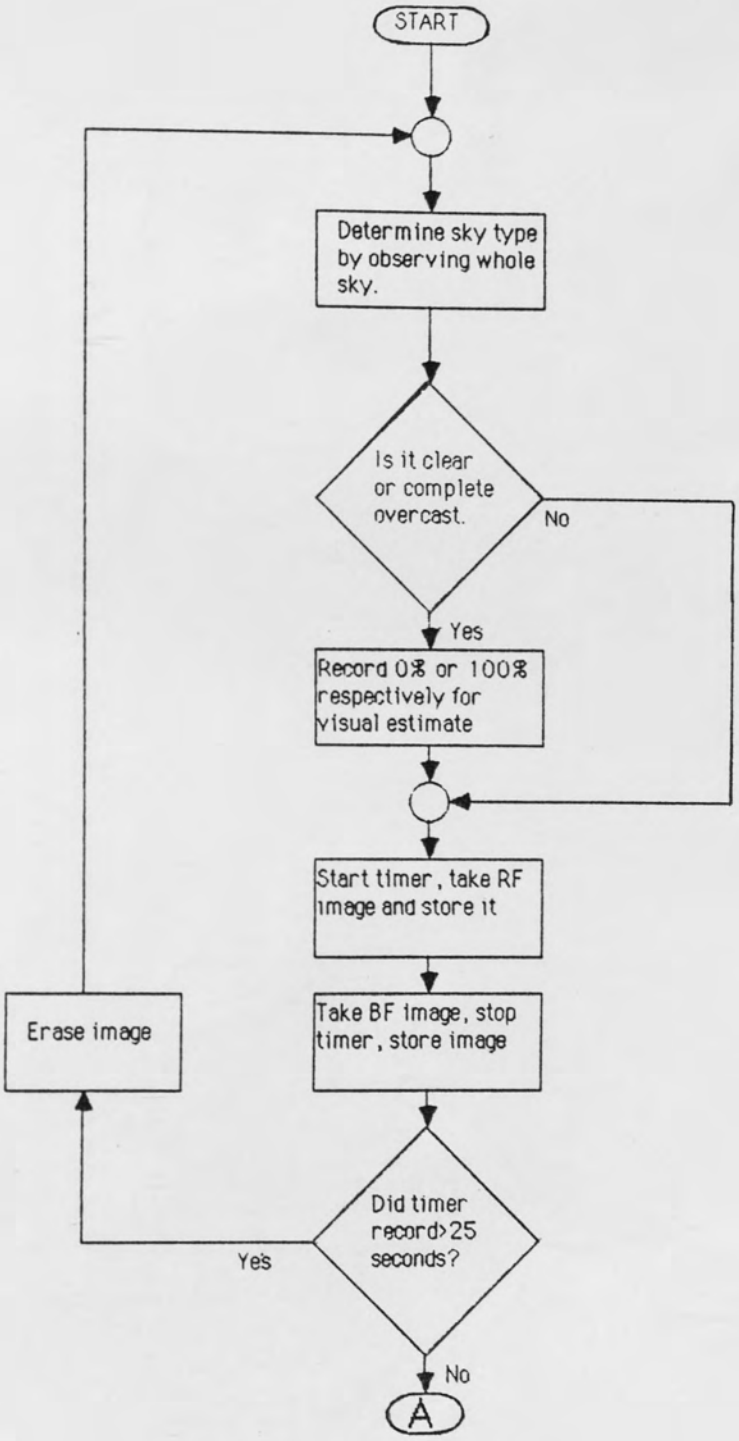
START
Determine sky type by observing whole sky.
Is it clear or complete overcast.
No
Yes
Record 0% or 100% respectively for visual estimate
Start timer, take RF image and store it
Take BF image, stop timer, store image
Did timer record>25 seconds?
Yes
Erase image
No
A

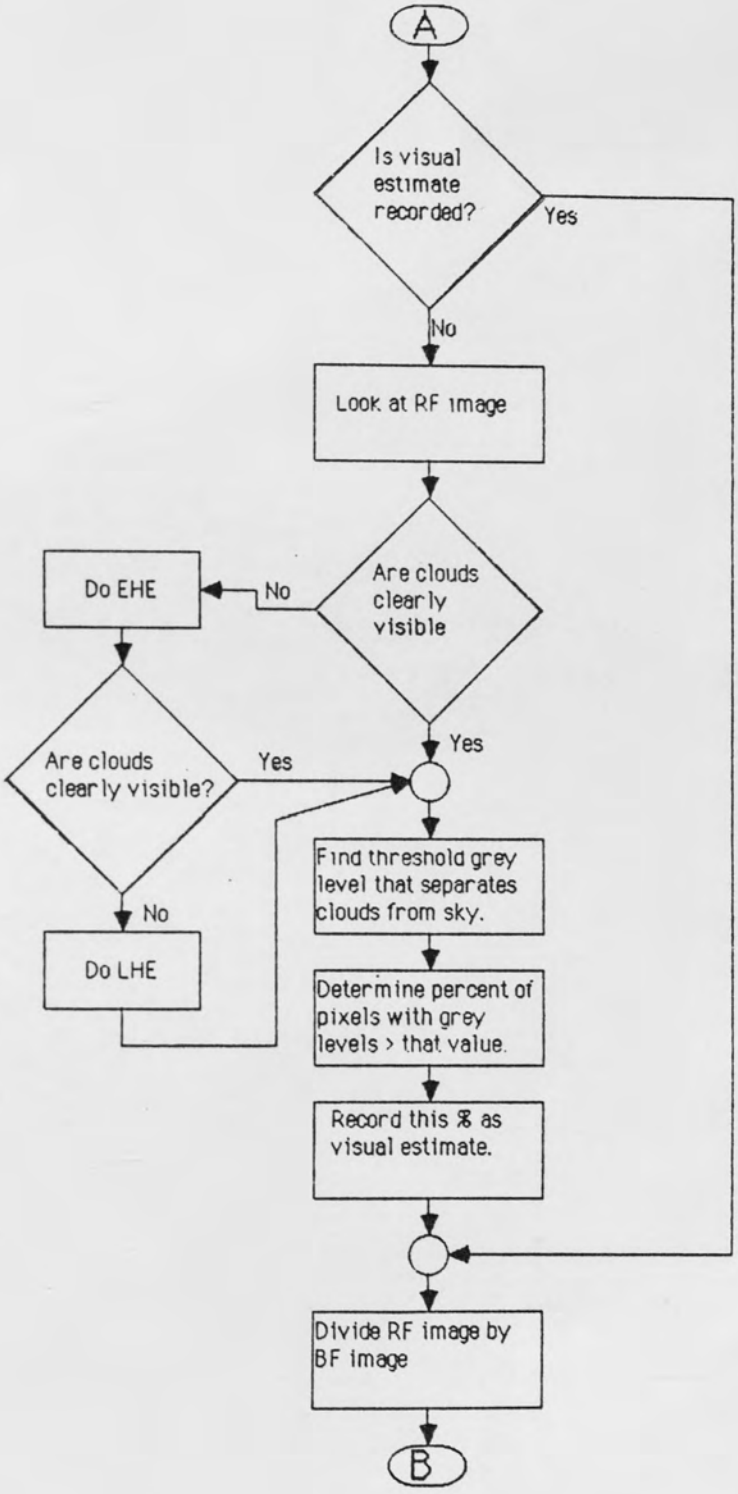
A
Is visual estimate recorded?
Yes
No
Look at RF image
Are clouds clearly visible
No
Do EHE
Yes
Are clouds clearly visible?
Yes
No
Do LHE
Find threshold grey level that separates clouds from sky.
Determine percent of pixels with grey levels > that value.
Record this % as visual estimate.
Divide RF image by BF image
B

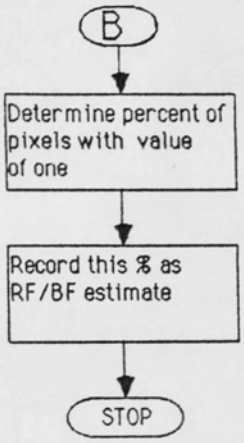
B
Determine percent of pixels with value of one
Record this % as RF/BF estimate
STOP

## REFERENCE LIST


ANSI 1967. American National Standard: Nomenclature and definitions for illuminating engineering, Z7.1-1967. New York: Illuminating Engineering Society.

Born, Max, and Wolf, Emil. 1959. Principals of Optics. New York: Pergamon Press.

Brumberger, H. et al. 1968. Light Scattering. Science and Technology. (November): 34-60.

Chandrasekhar, S. 1960. The equation of transfer. In Radiative Transfer, 1-52. New York: Dover Publications, Inc.

Chu, B. 1967. Molecular forces. New York: Wiley.

Coulson, Kinsell L. 1975. Solar radiation: Direct component in solar and terrestrial radiation, 39-83. New York: Academic Press.

Deirmendjian, D. 1969. Electromagnetic scattering or spherical polydispersions. New York: American Elsevier.

Dixon, Wilfrid J., and Massey, Frank J. 1969. Introduction to statistical analysis. New York: McGraw-Hill Book Company.

Dyckman, T.T., Smidt, S., and McAdams, A.K. 1969. Management decision making under uncertainty: An introduction to probability and statistical decision theory. London: The MacMillon Company, Collier-MacMillon Limited.

Frank, N.H. 1950. Introduction to electricity and optics, 2nd. ed. New York: McGraw-Hill.

Galligan, A.M. 1953. Variability of subjective cloud observations -I. AFCRC technical report 53-10. Cambridge, Massachusetts: Air Force Cambridge Research Center.

Gumprecht, R.O., and Sliepceich, C. M. 1951a. Tables of Ricatti-Bessel functions for large arguments and orders. Ann Arbor: Engineering Research Institute, University of Michigan.

Gumprecht, R.O., and Sliepceich, C. M. 1951b. Tables of scattering functions for spherical particles. Ann Arbor: Engineering Research Institute, University of Michigan.

Gumprecht, R. O., and Sliepceich, C. M. 1951c. Tables of first and second partial derivatives of Legendre polynomials. Ann Arbor: Engineering Research Institute, University of Michigan.

Hall, David J. 1976. An adaptive process for tracking clouds from satellite images. In Image Science Mathematics: Proceedings of the Symposium, Monterey, CA (10-12 November): 118.

Harrison, A.W., and Coombes, C.A. 1986. Comparison of infrared radiometric, observed and sunshine-derived cloud cover. Atmosphere-Ocean 24, no. 3: 283-291.

Holte, Ronald L., and Steven A. McKay. 1975. Tropical cloudiness from all-sky cameras on Barbados and adjacent Atlantic ocean. Journal of Applied Meteorology 14, no. 8 (December): 1437-1450.

IES. 1981. Handbook of Illuminating Engineering Society of North America. New York: Illuminating Engineering Society.

Johnson, Ronald W., and Wayne S. Hering. 1987. Automated visibility and cloud cover measurements with a solid-state imaging system. Atmospheric Visibility Technical Note No. 203A (April): 1-16.

Kerker, M. 1969. The scattering of light and other electromagnetic radiation. New York: Academic Press.

MacAdam, D.L. 1967. Editor's page: Nomenclature and symbols for radiometry and photometry. Journal of the Optical Society of America 57: 854.

McCluney, Ross 1987. The FSEC Fenstration Energy and Illumination Performance Research Program. Cape Canaveral, Florida: Florida Solar Energy Center. FSEC-PR-115-87.

Mie, G. 1908. A contribution to the optics of turbid media, especially colloidal metallic suspensions. Annals of Physics. Vol 25, no. 4, 377-445. Cited in Earl J. McCartney, Mie scattering by monodispersions and Mie scattering by atmospheric polydispersions in Scattering by molecules, and particles, 216-318. New York: John Wiley and Sons, 1976.

Penndorf, R. 1957. Tables of the refractive index for standard air and the Rayleigh scattering coefficient for the spherical region between 0.2 and 20.0, and their application to atmospheric optics. Journal of the Optical Society of America 47: 603-605.

Rayleigh, Lord. 1871. On the light from the sky, its polarization and color, and On scattering of light by small particles. Philadelphia Magazine. Vol. 41, 107-120, 274-279, 447-454. Cited in Earl J. McCartney, Rayleigh scattering by molecules in Scattering by molecules and particles, 176-215. New York: John Wiley and Sons, 1976.

Rayleigh, Lord. 1899. On the transmission of light through an atmosphere containing many small particles in suspension, and on the origin of the blue of the sky. Philadelphia Magazine. Vol 47, 375-384. Cited in Earl J. McCartney, Rayleigh scattering by molecules in Scattering by molecules and particles, 176-215. New York: John Wiley and Sons, 1976.

Stone, John M. 1963. Radiation and Optics. New York: McGraw-Hill Book Company, Inc.

van de Hulst, H.C. 1957. Light scattering by small particles. New York: Wiley.

Yellott, John I. 1983. Historical development of solar radiation measurements. In Daylight Availability Meeting Proceedings. Berkeley, California: Lawrence Berkeley Laboratory, University of California.